

Exploring the Most Extreme Gamma-Ray Blazars Using Broadband Spectral Energy Distributions

M. Láinez¹ *, M. Nieves-Rosillo^{2,3} **, A. Domínguez¹ ***, J. L. Contreras¹, J. Becerra González^{2,3}, A. Dinesh¹, and V. S. Paliya⁴

¹ IPARCOS and Department of EMFTEL, Universidad Complutense de Madrid, E-28040 Madrid, Spain

² Instituto de Astrofísica de Canarias, E-38205 La Laguna, Tenerife, Spain

³ Universidad de La Laguna, Dept. Astrofísica, E-38206 La Laguna, Tenerife, Spain

⁴ Inter-University Centre for Astronomy and Astrophysics (IUCAA), SPPU Campus, 411007, Pune, India

Received September 15, 1996; accepted March 16, 1997

ABSTRACT

Context. Extreme high-synchrotron peaked blazars (EHSPs) are rare high-energy sources characterised by synchrotron peaks beyond 10^{17} Hz in their spectral energy distributions (SEDs). Their extreme properties challenge conventional blazar emission models and provide a unique opportunity to test the limits of particle acceleration and emission mechanisms in relativistic jets. However, the number of identified EHSPs is still small, limiting comprehensive studies of their population and characteristics.

Aims. This study aims to identify new EHSP candidates and characterise their emission properties, including synchrotron peak frequencies, Compton dominance, and jet environments. It also examines how EHSPs fit within the broader framework of the blazar sequence, providing insights into their role in the population of active galactic nuclei.

Methods. A sample of 124 γ -ray blazars is analysed, selected for their high synchrotron peak frequencies and γ -ray emission properties, with a focus on sources showing low variability and good broadband data coverage. Their SEDs are constructed using archival multi-wavelength data from the SSDC SED Builder service, supplemented with recent *Swift*-UVOT, *Swift*-XRT, and *Fermi*-LAT observations. The SEDs are modelled with a one-zone synchrotron/synchrotron-self-Compton framework, classifying sources by synchrotron peak frequency. EHSP properties are compared to other blazar populations, and their detectability with the Cherenkov Telescope Array Observatory (CTAO) is assessed.

Results. We identify 66 new EHSP candidates, significantly expanding the known population. Their synchrotron peak frequencies are statistically higher than in previous studies, and they exhibit low Compton dominance, consistent with environments lacking strong external photon fields. A clear correlation between synchrotron peak frequency and the magnetic-to-kinetic energy density ratio is found, with the most extreme EHSPs nearing equipartition. Host galaxy emission is detected in many sources, but no significant differences are observed between elliptical and lenticular hosts. Finally, our analysis suggests that 9 high-synchrotron peaked/EHSPs could be observed by CTAO at $> 5\sigma$ (20 at $> 3\sigma$) in 20-hour exposures, a feasible integration time for Imaging Atmospheric Cherenkov Telescopes, highlighting their potential to improve studies of extreme jet physics and cosmology.

Key words. Radiation mechanisms: non-thermal – Gamma rays: galaxies – Galaxies: jets – Galaxies: active – BL Lacertae objects: general

1. Introduction

Active galactic nuclei (AGNs) are extreme cosmic sources, powered by matter accretion onto a supermassive black hole (SMBH, e.g., Combes 2021). Some develop relativistic jets extending to kiloparsec scales (e.g., Marsch 2010). Unification models classify radio-loud AGNs by jet viewing angle (e.g., Urry & Padovani 1995), with blazars, jets aligned close to our line of sight, dominating the extragalactic γ -ray sky (Abdollahi et al. 2020).

Blazars have broadband spectral energy distributions (SEDs) dominated by non-thermal emission from radio to γ rays (e.g., Fossati et al. 1998; Padovani 2017). Their SEDs feature a double-peaked structure: the lower-energy peak (infrared to X-ray) arises from synchrotron emission by relativistic jet electrons, while the origin of the higher-energy γ -ray peak remains

debated (e.g., Abdo et al. 2010), with both hadronic and leptonic processes proposed.

Leptonic models explain the higher-energy peak of blazar SEDs as inverse Compton (IC) scattering, where high-energy electrons interact with low-energy photons (e.g., MAGIC Collaboration et al. 2020, 2021). This occurs mainly through synchrotron-self-Compton (SSC), where electrons scatter their own synchrotron photons (e.g., Maraschi et al. 1992; Finke et al. 2008), and external Compton, where electrons scatter external photons from sources like the cosmic microwave background, broad-line region (BLR), dusty torus, disk, stars, or different jet layers (e.g., Sikora et al. 1994; van den Berg et al. 2019). Hadronic models instead attribute γ -ray emission to high-energy proton interactions with ambient matter or radiation fields and to synchrotron radiation from relativistic protons in strong magnetic fields (e.g., Mannheim & Biermann 1992; Böttcher et al. 2013, and references therein). Lepto-hadronic models combine both leptonic and hadronic processes (e.g., Mücke et al. 2003; Paliya et al. 2018). The main acceleration mechanisms proposed

* e-mail: malainez@ucm.es

** e-mail: mireia.nieves@iac.es

*** e-mail: alberto.d@ucm.es

for ultra-relativistic particles in blazar jets include shock acceleration via repeated shock crossings and magnetic turbulence (e.g., Kirk et al. 1998; Tavecchio et al. 2020), as well as magnetic reconnection (e.g., Sironi & Spitkovsky 2014) and stochastic acceleration (e.g., Blandford & Eichler 1987; Liu et al. 2017).

Blazars are classified based on their optical spectra into flat spectrum radio quasars (FSRQs) and BL Lacertae objects (BL Lacs). FSRQs exhibit strong, broad emission lines ($EW > 5 \text{ \AA}$), while BL Lacs have an almost featureless continuum (e.g., Marcha et al. 1996), indicating that external photon sources like the BLR, dusty torus, or disk are subdominant, with emission mainly from synchrotron/SSC (e.g., Ghisellini et al. 2011). In the most extreme BL Lacs, where the synchrotron peak is at higher frequencies, the host galaxy’s thermal emission becomes visible in the optical/ultraviolet (UV) range, allowing absorption lines to be detected. Blazars are also categorized by their synchrotron peak frequency (e.g., Padovani & Giommi 1995; Abdo et al. 2010), from low-synchrotron peaked (LSP, $\nu_{\text{sync}}^{\text{peak}} < 10^{14} \text{ Hz}$) to intermediate (ISP, $10^{14} \text{ Hz} \leq \nu_{\text{sync}}^{\text{peak}} < 10^{15} \text{ Hz}$), high (HSP, $10^{15} \text{ Hz} \leq \nu_{\text{sync}}^{\text{peak}} < 10^{17} \text{ Hz}$), and extreme high-synchrotron peaked (EHSP, $\nu_{\text{sync}}^{\text{peak}} \geq 10^{17} \text{ Hz}$), with peaks often reaching the X-ray band.

Blazars often show variability on timescales from minutes to years, differing across energy bands (e.g., Urry 1996; Marscher et al. 2008). HSPs and EHSPs vary significantly in X-rays but show little to no large-scale variability in the γ -ray band, whereas LSPs and ISPs are generally more variable at high-energy (HE, $100 \text{ MeV} < E < 100 \text{ GeV}$) γ rays. This pattern may result from the low γ -ray luminosity of HSPs and EHSPs, as their apparent lack of variability could stem from the limited sensitivity of *Fermi*-LAT and Imaging Atmospheric Cherenkov Telescopes (IACTs) to low-flux sources (Ackermann et al. 2011).

FSRQs, the most luminous blazars, are mainly LSPs, while higher synchrotron peak frequency blazars are mostly lower-luminosity BL Lacs (e.g., Giommi et al. 2012). This anti-correlation between luminosity and synchrotron peak frequency defines the *blazar sequence* (Fossati et al. 1998; Ghisellini et al. 2017), though observational biases and sample selection may challenge its validity (e.g., Padovani 2007; Giommi et al. 2012; Padovani et al. 2022).

EHSPs, with radiatively inefficient accretion disks, occupy the end of the blazar sequence (e.g., Ghisellini et al. 2011). Their extreme synchrotron peak frequencies challenge standard models, requiring extreme conditions for the ultra-relativistic particles responsible for their emission (e.g., Biteau et al. 2020). Studying EHSPs enhances our understanding of jet acceleration and non-thermal emission. Their high energies (up to tens of TeV, Biteau et al. 2020) make them valuable for cosmological studies, including the extragalactic background light (EBL, e.g., Domínguez & Ajello 2015; Domínguez et al. 2019; Gréaux et al. 2024), blazar evolution (e.g., Ajello et al. 2014), the extragalactic γ -ray background (e.g., Ajello et al. 2015; Paliya et al. 2019), and the intergalactic magnetic field (e.g., Bonnoli et al. 2015). As potential very-high-energy (VHE, $E > 100 \text{ GeV}$) emitters, they are prime targets for IACTs. Although blazars, particularly BL Lacs, dominate the extragalactic γ -ray sky, only a few dozen EHSPs are known (Nievas Rosillo et al. 2022; Acciari et al. 2020).

This work examines 124 blazars selected as possible EHSPs by modelling their broadband SEDs with a one-zone synchrotron/SSC model to classify them by synchrotron peak fre-

quency and assess their physical properties within the broader blazar population.

The paper is organised as follows: Section 2 describes source selection and multi-wavelength data, Section 3 details SED modelling, and Section 4 discusses EHSP properties. Section 5 presents detectability predictions with Cherenkov Telescope Array Observatory (CTAO), and Section 6 provides a summary and conclusions.

Throughout this paper, we adopt the following cosmological parameters: Hubble constant $H_0 = 67.8 \text{ km s}^{-1} \text{ Mpc}^{-1}$, matter density parameter $\Omega_{M,0} = 0.307$, baryon density parameter $\Omega_{b,0} = 0.0483$, cosmic microwave background temperature $T_{\text{CMB},0} = 2.725 \text{ K}$, effective number of relativistic degrees of freedom $N_{\text{eff}} = 3.05$, and a total neutrino mass sum of 0.06 eV .

2. Sample selection and multi-wavelength data

2.1. Source selection

We select blazars from the Second Brazil-ICRANet Gamma-ray Blazars catalogue (2BIGB catalogue; Arsioli et al. 2020), which contains 1160 γ -ray blazars along with their γ -ray SEDs. These SEDs were obtained from the first 11 years of observations by the *Large Area Telescope* (LAT) aboard the *Fermi Gamma-ray Space Telescope*, a space-based instrument designed to detect γ rays in the energy range from approximately 20 MeV to over 300 GeV (Atwood et al. 2009). The 2BIGB catalogue was produced through a γ -ray likelihood analysis of all sources in the 3HSP catalogue (Chang et al. 2019), which remains the largest collection of HSPs, EHSPs, and blazar candidates of uncertain type (BCUs, that is, sources detected by *Fermi*-LAT that show characteristics typical of blazars, as a double peaked SED, but lack definitive classification as either BL Lac or FSRQ).

To avoid contamination of diffuse emission from the Galactic plane, we select only blazars located at high latitudes ($|b| > 10^\circ$). We also require that all sources in our sample have a redshift estimate, even if photometric, along with flux measurements in the optical/UV, X-ray, and γ -ray bands. With these criteria, we obtain a preliminary sample of 657 γ -ray blazars. We cross-reference these sources with the *Fermi*-LAT Fourth Source catalogue Data Release 4 (4FGL-DR4, Ballet et al. 2023), which lists γ -ray sources detected by *Fermi*-LAT over its first 14 years.

Since we use archival data from multiple telescopes to reconstruct the broadband SEDs of the selected blazars, and these data are not always taken simultaneously, additional cuts are applied to select sources with low variability across different energy bands. The variability index from the 4FGL-DR4 catalogue is used to identify sources with low variability in the *Fermi*-LAT energy range. This index is calculated for each source as twice the sum of the log-likelihood differences between the flux in various time intervals and the average flux over the entire catalogue interval (Ajello et al. 2020). Only sources with a variability index below 27.69, the 99% confidence threshold in 4FGL-DR4, are included.

To assess the variability of the sources in the X-ray band, data from the X-ray Telescope aboard the Neil Gehrels *Swift* Observatory (*Swift*-XRT, Burrows et al. 2005) are analysed to construct light curves. A Bayesian block analysis (Scargle et al. 2013), as implemented in *astropy* (Astropy Collaboration et al. 2022, 2018, 2013), is used to distinguish sources with a single block (likely non-variable) from those with multiple blocks (variable). We adopt a false probability $p_0 = 0.01$ and a systematic uncertainty of 10%. Only sources with a single Bayesian block in their light curve are included, resulting in 124 se-

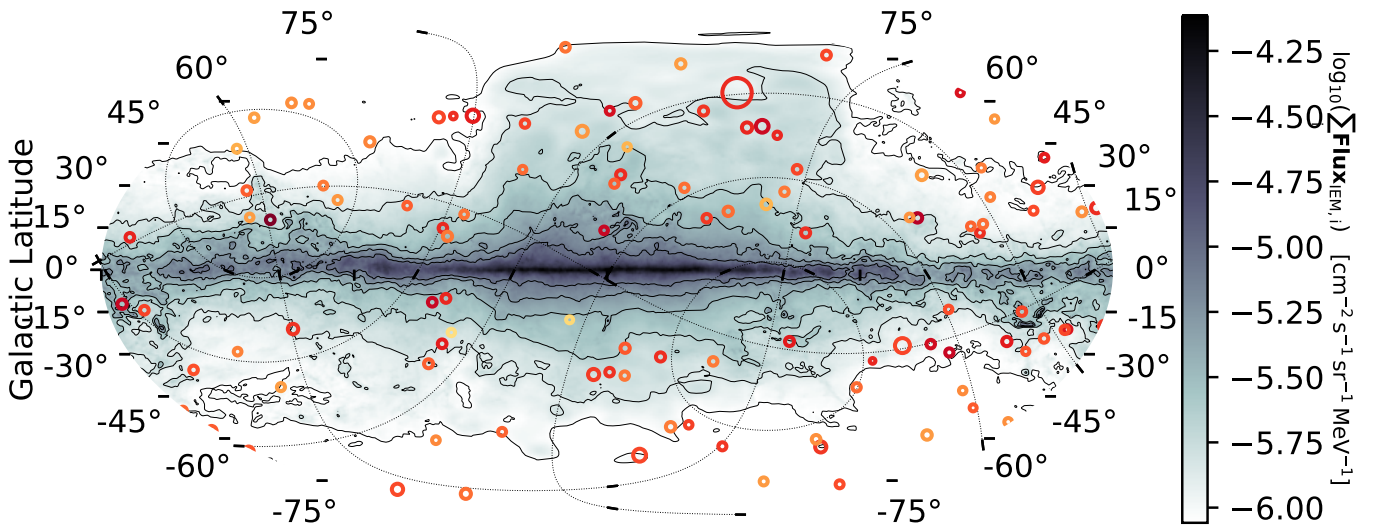


Fig. 1: Sky location of 124 sources selected for our analysis in Galactic coordinates. Each circle represents a source, with its colour corresponding to the flux (in log scale, with red tones for brighter sources). The size of the circle is proportional to $1/\sqrt{z}$. For reference, the diffuse γ -ray emission from the Galaxy is shown in blue tones.

lected blazars. However, gaps in the temporal sampling may affect variability estimates. In general, variability studies benefit from frequent and continuous monitoring, which allows for better characterization of the synchrotron component. However, for EHSPs, the optical/UV bands often contain a significant contribution from the host galaxy’s thermal emission (e.g., Scarpa et al. 2000), reducing the sensitivity to AGN variability. As a result, no variability-based selection criteria are applied in this energy range. A skymap showing the distribution of the 124 selected blazars is presented in Figure 1.

We do not apply any additional requirements regarding the class of the sources in 4FGL. Of the 124 sources in the final sample, 93 are classified as BL Lacs in the 4FGL-DR4 catalogue (Ballet et al. 2023), one as an FSRQ (4FGL J0132.7–0804, although it is likely misclassified; see Section 4.1), 1 as a radiogalaxy (4FGL J1518.6+0614), and 29 as BCUs. Most sources in the sample are BL Lacs since the blazars listed in the 3HSP catalogue show characteristics commonly associated with HSP and EHSP blazars. Figure 2 shows the dependence of the spectral index on flux and the variability index, as well as the relationship between the variability index and flux, for all sources in our sample and all sources classified as BL Lacs or FSRQs in the 4FGL catalogue. As expected, the sources selected for our study tend to have harder spectra than is typically found in FSRQs, as most of them belong to the BL Lac class.

The redshift distribution of the blazar sample is shown in Figure 3. They come from the 2BIGB (Arsioli et al. 2020) and 4LAC-DR3 (Ajello et al. 2020, 2022) catalogues, as well as from Goldoni (2021) and Paliya et al. (2021). Of these, 44 (35.5%) are from 4LAC, which does not specify whether they are spectroscopic or photometric, while 38 (30.6%) from 2BIGB are all photometric. The remaining redshifts, 33 (26.6%) from Paliya et al. (2021) and 9 (7.3%) from Goldoni (2021), are spectroscopic. Most of the sources in our sample ($\sim 86\%$) have a redshift of $z < 0.5$, although some sources reach much higher redshifts, with the farthest blazar in the sample located at $z = 2.075$ (4FGL J0323.7–0111, associated with 1RXS J032342.6–011131), though this redshift, given in 4LAC, may

be uncertain as the optical spectrum of the associated source is continuum-dominated.

2.2. Multi-wavelength data

For the construction of the broadband SEDs of all sources in the sample, we gather data from various telescopes covering different energy bands. In the X-ray band, data from *Swift*-XRT are incorporated into the broadband SEDs of the sample blazars, using our own analysis of the data. We use the UKSSDC XRT-prods Python API¹ (Evans et al. 2009, 2007), which retrieves high-level spectral data for the source and background regions along with the instrument response functions. Spectral parameters and flux points are then extracted with XSPEC (Arnaud 1996). In the optical/UV range, we also include data from the UV/Optical Telescope aboard the Neil Gehrels *Swift* Observatory (*Swift*-UVOT, Roming et al. 2005), which we analyse using an automated tool built on the official HEASARC *uvot-product* package.

In the HE γ -ray band, we include flux data from *Fermi*-LAT available in the 4FGL-DR4 catalogue for eight energy bins. The only blazar in our sample detected in the VHE γ -ray band is 4FGL J0013.9–1854 (associated with SHBL J001355.9–185406), for which we also include the H.E.S.S. data provided in the Spectral TeV Extragalactic catalogue (STeV-Cat; Gréaux et al. 2023).

Additionally, for each source, we incorporate multi-wavelength archival data from the Space Science Data Center (SSDC SED Builder service², an online tool for downloading data collected by multiple instruments over several decades. The SSDC SED Builder is used to extract historical data for each blazar across all bands except γ rays. Since our study focuses on low-variability sources, we do not apply any time constraints on the SSDC data to exclude potential flaring periods.

¹ <https://www.swift.ac.uk/API>

² <https://tools.ssdc.asi.it/SED/>

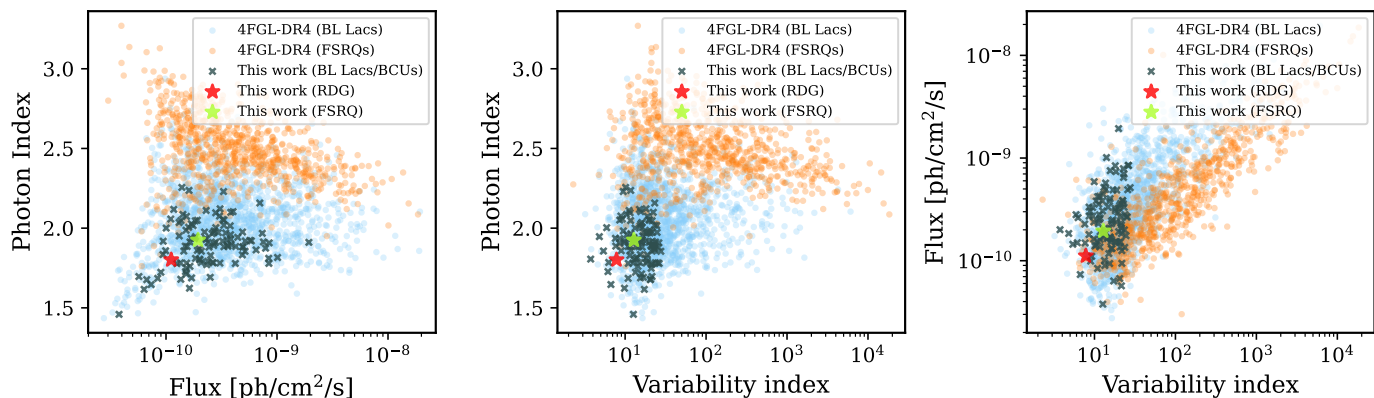


Fig. 2: The 124 sources in our sample compared to all BL Lacs and FSRQs in the 4FGL-DR4 catalogue. Left: Photon spectral index versus the integral photon flux from 1 to 100 GeV. Middle: Photon spectral index versus the variability index. Right: Variability index versus the integral photon flux from 1 to 100 GeV. The photon index, flux, and variability index values are from the 4FGL-DR4 catalogue. We represent all the BL Lac sources from the 4FGL-DR4 catalogue with blue circles and the FSRQs with orange circles. The sources selected for this work are marked with dark crosses, the radiogalaxy of the sample (4FGL J1518.6+0614) is marked with a red star, and the FSRQ (4FGL J0132.7-0804) is marked with a green star.

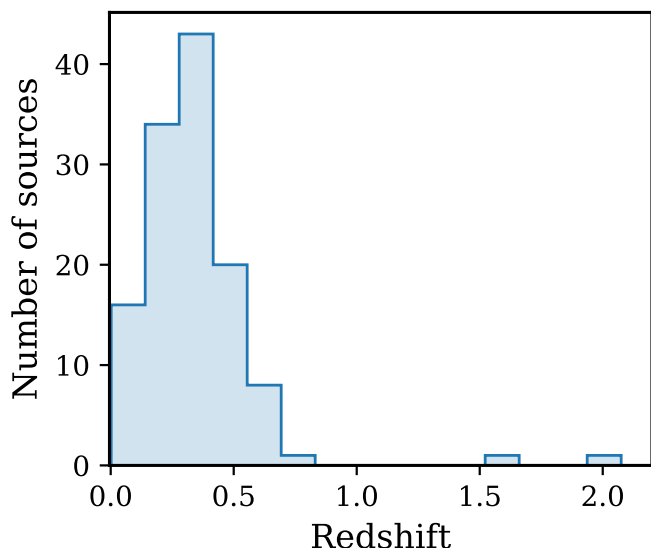


Fig. 3: Redshift distribution of the 124 sources of the sample.

3. Methodology: Broadband SED modelling

3.1. Host galaxy emission

Since EHSP blazars have low non-thermal flux at optical/UV energies and their synchrotron peak occurs at higher frequencies, the host galaxy’s thermal emission is often prominent in the optical range of their SEDs. Therefore, before modelling the broadband SEDs, we fit different host galaxy models to the data in the optical range to determine the best-fitting model. For this purpose, we use four host galaxy templates from the SWIRE Template Library³ (Polletta et al. 2007). The host galaxies of most blazars are elliptical galaxies, characterised by old stellar populations and low star formation rates (Urry et al. 2000; Paliya et al. 2021). Lenticular galaxies, while distinct in structure, share these same characteristics and are indistinguishable from ellipti-

³ http://www.iasf-milano.inaf.it/~polletta/templates/swire_templates.html

cals in the optical band, specifically in the range where we fit the host galaxy templates (7×10^{13} Hz to 10^{15} Hz). For this reason, the templates that we employ, shown in Figure 4, correspond to elliptical galaxies of 2 Gyr, 5 Gyr, and 13 Gyr, and to a lenticular galaxy. The best-fit host galaxy model is considered to be the one for which the lowest χ^2 value is obtained in the optical range (7×10^{13} Hz to 10^{15} Hz). We then assume black-body emission and, by applying Wien’s displacement law, estimate the approximate value of the temperature of the host galaxy. The host galaxy emission is generally not considered a significant source of seed photons for the external Compton process, and therefore, its contribution to the external Compton emission at high energies can be considered negligible. Thus, this contribution is not included in the broadband SED modelling. External Compton emission can also arise from the IR photons of the dusty torus. However, for EHSPs, this contribution is usually negligible, and, therefore, we exclude it from our modelling.

3.2. Synchrotron and inverse Compton emission

Once the host galaxy template that best fits the optical data is identified, the broadband SED modelling is conducted using a one-zone synchrotron/SSC model combined with the best-fit host galaxy model and all the data described in Section 2.2. In the absence of flaring states, the SEDs of HSPs and extreme blazars are well described by a simple one-zone SSC model (e.g., Sol & Zech 2022), where the higher energy peak results from inverse Compton scattering of the electron population with photons produced by the synchrotron process. For these blazars, the external Compton component is typically negligible due to the relatively simple environments surrounding their jets, which lack a dusty torus or a BLR to supply the photons necessary for the external Compton mechanism (e.g., Ghisellini et al. 2011; Falomo et al. 2014). Therefore, a one-zone SSC model is generally sufficient to describe their SEDs (Celotti & Ghisellini 2008).

3.3. Model assumptions and fitting

In the one-zone SSC model, both synchrotron and inverse Compton components are assumed to originate from the same region. For the source geometry, we adopt the simplest scenario where

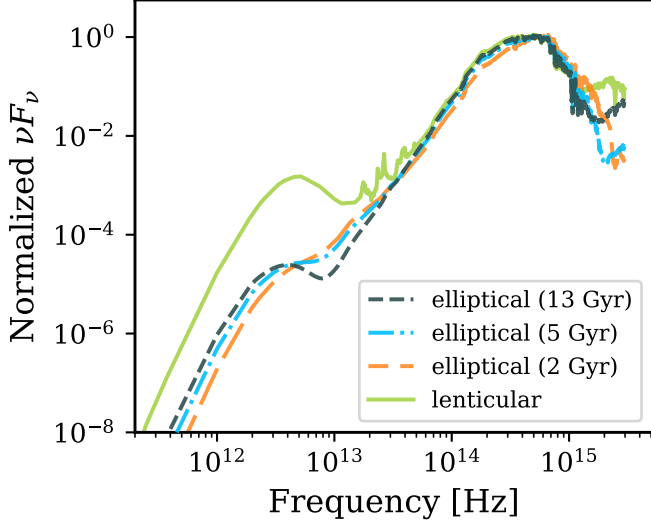


Fig. 4: Templates from the SWIRE Template Library used for modelling the host galaxy emission, corresponding to elliptical galaxies of 2 Gyr, 5 Gyr, and 13 Gyr, and to a lenticular galaxy.

the emission is produced in a single spherical region or blob of radius R , located within the jet at a distance R_H from the central SMBH. This region is filled with ultra-relativistic electrons moving with a bulk Lorentz factor Γ . In blazars, the observed emission is highly beamed and Doppler-boosted due to the blob's relativistic motion and the jet's small angle relative to our line of sight. The magnetic field B is considered homogeneous within the blob. The electron population is modelled with a broken power-law distribution: a lower energy population with spectral slope p_1 and Lorentz factors between γ_{\min} and γ_{break} , and a higher energy population with spectral slope p_2 and Lorentz factors between γ_{break} and γ_{\max} . During the fitting, following the methodology from Nievas Rosillo et al. (2022), γ_{\min} is fixed at 10^3 , while γ_{\max} , γ_{break} , p_1 , and p_2 are treated as free parameters.

The SED modelling is performed using the `JetSeT v1.3.0` package (Tramacere 2020; Tramacere et al. 2011, 2009), first running the `lsb` (least square bound scipy) minimiser followed by the `minuit` minimiser. To reduce the degrees of freedom in the model, some parameters are fixed to typical values for EHSP-like blazars, following Nievas Rosillo et al. (2022). The radius of the emitting region is set to $R = 10^{16}$ cm, the distance of the blob from the central black hole is set to $R_H = 2 \times 10^{18}$ cm, and the bulk Lorentz factor is fixed at $\Gamma = 20$. Adjusting these parameters impacts SED modelling: a larger emitting region lowers radiation energy density, affecting synchrotron and inverse Compton peaks; changing the SMBH distance alters jet dynamics and energy transfer; varying the Lorentz factor modifies observed flux through Doppler boosting. Despite these sensitivities, the parameters reflect standard EHSP models and general high-frequency blazar behaviour. With these assumptions, seven free parameters remain in the model: the magnetic field strength B , the electron density N , the spectral indices of the low- and high-energy particles p_1 and p_2 , the maximum Lorentz factor γ_{\max} , the break Lorentz factor γ_{break} , and the jet viewing angle θ . The Doppler boosting factor δ is also treated as a free parameter, as it depends on the jet viewing angle θ . Its dependence on the bulk Lorentz factor and the jet viewing angle is given by:

$$\delta = \frac{1}{\Gamma(1 - \beta \cos \theta)}, \quad \beta = v/c \quad (1)$$

where β is the speed of the jet in terms of the speed of light.

We fit the data in the range from 5×10^{10} Hz to 10^{27} Hz, excluding the radio emission, as it is often believed to originate from a region much larger than the compact region responsible for the rest of the broadband SED. Additionally, at radio frequencies, synchrotron self-absorption becomes significant and may suppress low-frequency emission (e.g., Tavecchio et al. 1998). EBL absorption of γ rays is taken into account, with attenuation becoming significant above ~ 100 GeV for nearby sources but affecting progressively lower energies at higher redshifts, starting around ~ 30 GeV for $z \sim 1$. The EBL, composed of the accumulated and redshifted light from all galaxies, stars, and interstellar dust in the universe, attenuates γ rays through pair-production interactions with high-energy photons. This attenuation is incorporated using the optical depths from Domínguez et al. (2024b), based on the EBL model by Saldana-Lopez et al. (2021). An example of the broadband SED of one source from the sample fitted with this model is shown in Figure 5. All multi-wavelength SEDs of the 124 sample sources with their best-fit models are presented in Appendix A.

Even after applying cuts to the initial sample to exclude potential variable sources in the X-ray band, when considering data from different instruments some sources still show flux dispersion. This variability in X-ray flux could have influenced the SED modelling. To ensure reliable results for the EHSP blazar properties derived here, we exclude sources with poor fitting results by selecting only those with $\chi^2/\text{dof} < 1.5$. The χ^2 was calculated using only the X-ray and γ -ray bands, considering all data points above 10^{16} Hz, since the radio and optical ranges show more dispersion. In total, 113 sources meet this requirement, resulting in the exclusion of 11 sources. These 11 sources are not considered when deriving the general properties of our blazar sample, as shown in Figures 6, 7, 8, 9, 10, 11, and 12.

4. Results and discussion

4.1. Broadband SED modelling results

The best-fit parameters resulting from the SED modelling performed for each source in the sample are provided in Appendix B, Table B.1⁴. The SED modelling also allows us to calculate the synchrotron peak frequency, $\nu_{\text{sync}}^{\text{peak}}$, and the Compton dominance (CD), which are listed in Table B.2 for each source. CD is a parameter used in the study of blazars and other AGNs to describe the relative strength of inverse Compton emission compared to synchrotron emission in their spectral energy distributions. It plays a crucial role in understanding the physical environment of the jet, including the balance of magnetic and particle energy densities, the photon fields driving the inverse Compton process, and the overall energy dissipation mechanisms in the blazar (e.g., Paliya et al. 2021).

We find that out of the 113 sources in the sample with good fits, 66 have $\nu_{\text{sync}}^{\text{peak}} \geq 10^{17}$ Hz and could therefore be classified as EHSPs according to our results. Of the remaining sources, 41 have 10^{15} Hz $\leq \nu_{\text{sync}}^{\text{peak}} < 10^{17}$ Hz and could be classified as HSPs. However, six sources have 10^{14} Hz \leq

⁴ We make publicly available at Zenodo all the SED fluxes and the results from the SED fits (insert link) and at <https://www.ucm.es/blazars/>.

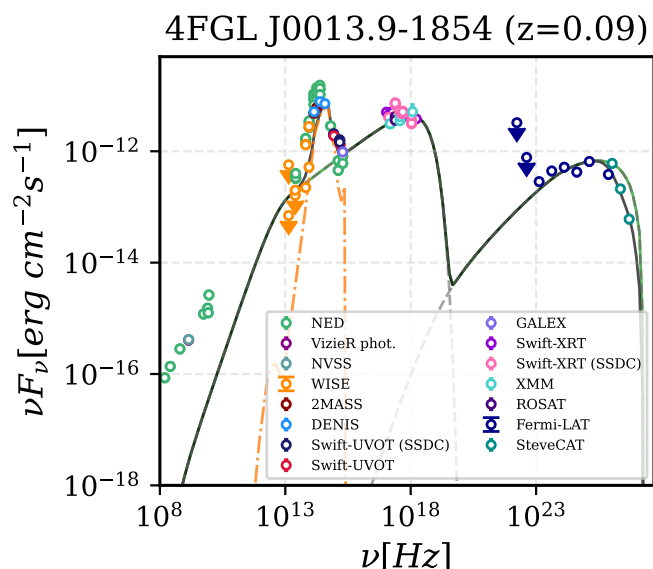


Fig. 5: Multi-wavelength emission of blazar 4FGL J0013.9–1854 modelled using a one-zone SSC model and a 13 Gyr old elliptical galaxy template for the host. The fluxes used to reconstruct the SEDs are shown as coloured points. The synchrotron and SSC emission from the best-fit model (dashed-grey line), the host galaxy emission (orange), the total intrinsic emission summing all components (solid-green line), and the observed emission after accounting for EBL absorption (solid-black line) are displayed.

$\nu_{\text{sync}}^{\text{peak}} < 10^{15}$ Hz, placing them in the ISP class of blazars. These sources are: 4FGL J0146.9–5202, 4FGL J1241.8–1456, 4FGL J1311.0+0034, 4FGL J1340.8–0409, 4FGL J1440.9+0609, and 4FGL J1534.8+3716. The redshift distributions of EHSPs and HSPs/ISPs show no significant differences, providing no clear evidence of an evolutionary connection in our sample (Beckmann et al. 2003; Ajello et al. 2014). However, this result may be influenced by redshift uncertainties, particularly those from photometric estimates.

For the jet viewing angle, we obtain values of $\theta < 12^\circ$, with 85% of the sources having $\theta < 8^\circ$. This corresponds to Doppler factors between ~ 2 and 40, typical for blazars due to their jets being closely aligned with our line of sight. For the maximum Lorentz factor γ_{max} , we find values ranging from 2.9×10^5 to 4.6×10^8 . Determining γ_{max} is challenging due to the lack of measurements between 10^{18} Hz and $\sim 10^{20}$ Hz, the gap between NuSTAR and *Fermi*-LAT energy ranges, which may result in γ_{max} values larger than expected.

Figure 6 shows the relationship between CD, magnetic field strength, and synchrotron peak frequency for the 113 sources with good fitting results. Sources with lower synchrotron peak frequencies generally have lower magnetic field values and higher CD, while the most extreme sources (with the highest synchrotron peak frequencies) display higher magnetic field values and lower CD. Figure 7 presents the CD distribution for the EHSP and HSP/ISP candidates in our sample, showing that EHSP candidates typically have lower CD values than less energetic sources, as demonstrated by Paliya et al. (2021). However, all sources in our sample have modest CD, with the highest being $\text{CD} = 3.2$, corresponding to an HSP source (4FGL J1419.3+0444, $\nu_{\text{sync}}^{\text{peak}} = 1.0 \times 10^{16}$ Hz) based on our results. In

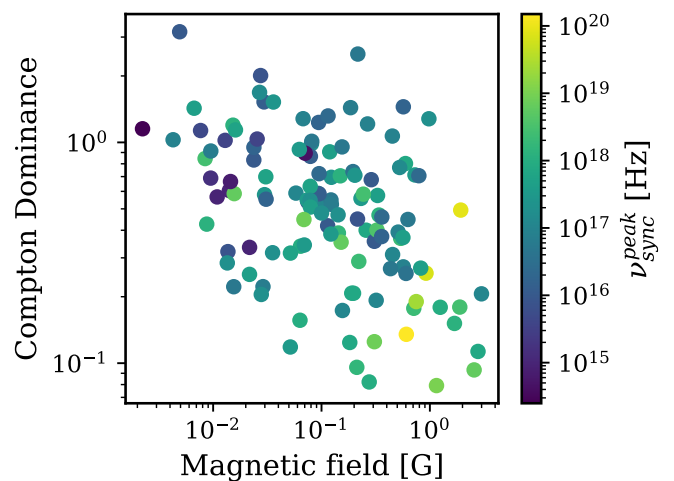


Fig. 6: CD as a function of the magnetic field for the 113 sources in the sample with a good fitting result. The colour scale represents the synchrotron peak frequency.

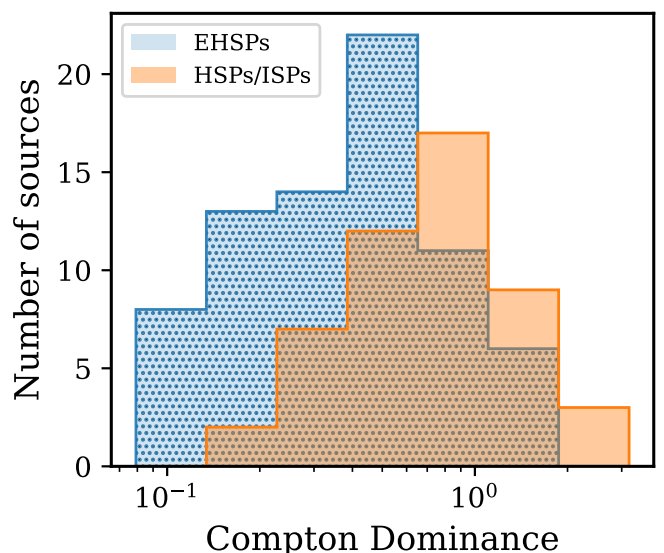


Fig. 7: CD distribution of the sources in the sample with $\nu_{\text{sync}}^{\text{peak}} \geq 10^{17}$ Hz (EHSPs, in blue) and $\nu_{\text{sync}}^{\text{peak}} < 10^{17}$ Hz (HSPs/ISPs, in orange).

contrast, the EHSP candidate with the highest CD value has $\text{CD} = 1.5$ (4FGL J1719.3+1205).

Out of the 113 sources with good fits, 28 overlap with those in Paliya et al. (2021), which catalogues 1077 γ -ray blazars or BCUs detected by *Fermi*-LAT with available optical spectra or measurements of host galaxy bulge magnitude, central SMBH mass, or disk luminosity. Figure 8 compares our results for CD and the synchrotron ($\nu_{\text{sync}}^{\text{peak}}$) and inverse Compton ($\nu_{\text{IC}}^{\text{peak}}$) peak frequencies for these 28 sources with those from Paliya et al. (2021). Their model does not account for host galaxy emission, potentially increasing the modelled non-thermal synchrotron component. This could partly explain why our $\nu_{\text{sync}}^{\text{peak}}$ values are systematically higher by a factor around 6, although a small contribution may arise from the inherent uncertainty introduced by the manual fitting procedure and differences between

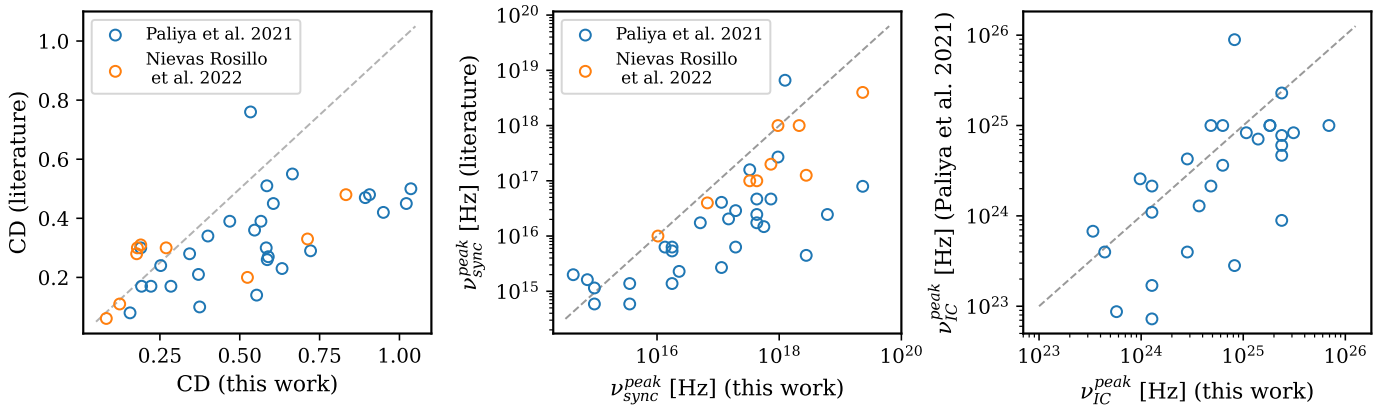


Fig. 8: The CD, synchrotron peak frequency, and inverse Compton peak frequency obtained in this work are compared with those reported by Paliya et al. (2021) for the 28 overlapping sources. The synchrotron peak frequency $\nu_{\text{sync}}^{\text{peak}}$ and CD obtained in this work are also compared with the $\nu_{\text{sync}}^{\text{peak}}$ and CD values from Nieves Rosillo et al. (2022) for the 9 sources present in both samples. The dashed grey line indicates the one-to-one correspondence.

the criteria adopted in each work, the data selection or the modelling codes.

This difference in $\nu_{\text{sync}}^{\text{peak}}$ directly impacts CD, which depends on the balance between synchrotron and inverse Compton emissions. Our CD values are consistently higher than those in Paliya et al. (2021), reflecting the weaker synchrotron component. In contrast, $\nu_{\text{IC}}^{\text{peak}}$ shows less deviation between the studies, suggesting it is less sensitive to modelling assumptions. However, this stability in $\nu_{\text{IC}}^{\text{peak}}$ does not offset the influence of the higher $\nu_{\text{sync}}^{\text{peak}}$ on CD.

Additionally, Figure 8 compares our $\nu_{\text{sync}}^{\text{peak}}$ and CD values with those from Nieves Rosillo et al. (2022), based on 22 2BIGB catalogue sources classified as BCU in 4FGL. Nine sources overlap between the two samples, showing better agreement than with Paliya et al. (2021), likely due to Nieves Rosillo et al. (2022) including a blackbody component to account for host galaxy emission. Still, our $\nu_{\text{sync}}^{\text{peak}}$ values remain systematically a factor of 3 higher, highlighting the existing systematic uncertainties arising from the modelling techniques used in these works.

In Figure 9, the CD distribution of our sample sources is shown, compared with that of the emission-line and absorption-line blazars from Paliya et al. (2021). The sources selected for this work appear to lie at the low end of the absorption-line blazar sample, suggesting that our sources can be classified within this subset of blazars. This population primarily consists of BL Lacs, whose spectra show absorption lines attributed to the stellar population of the host galaxy, while the emission-line blazars are typically identified as FSRQs. Note that blazar classification as absorption-line or emission-line objects depends on the source state, as even BL Lacs can display emission lines when the jet is not in a high state. Moreover, our predominantly EHSP sample shows higher CD values than their absorption-line blazars, suggesting greater radiative efficiency and stronger intrinsic absorption. While such absorption would typically shift the synchrotron peak to lower frequencies, our sources maintain high synchrotron peak values.

Furthermore, a correlation between accretion luminosity (L_{disk}) and CD in blazars was found by Paliya et al. (2021, shown in Figure 11 of that work), suggesting that blazars with high CD tend to be more luminous. In particular, emission-line blazars generally have $\text{CD} > 1$ and $L_{\text{disk}}/L_{\text{Edd}} > 0.01$, while absorption-

line blazars typically have $\text{CD} < 1$ and $L_{\text{disk}}/L_{\text{Edd}} < 0.01$. Based on these findings and given that most of the EHSP candidates in our sample show CD values of $\text{CD} \lesssim 1$, we expect these blazars to generally have L_{disk} values in Eddington units of $L_{\text{disk}}/L_{\text{Edd}} \leq 0.01$. Therefore, they can be classified as low-Compton-dominated (LCD) objects, according to the classification proposed by Paliya et al. (2021). In contrast, more Compton-dominated blazars, primarily FSRQs, are typically classified as high-Compton-dominated (HCD) objects. Hence, we conclude that our blazar sample mainly consists of LCD objects, with no emission lines and low accretion activity.

The FSRQ and the radiogalaxy in our sample, 4FGL J0132.7–0804 (PKS 0130–083) and 4FGL J1518.6+0614 (TXS 1516+064), respectively, both have $\text{CD} < 1$. Specifically, the results obtained are $\text{CD} = 0.27$ for 4FGL J0132.7–0804 and $\text{CD} = 0.12$ for 4FGL J1518.6+0614. Following the correlation derived in Paliya et al. (2021), these low CD values suggest that these two sources have low accretion activity or that the emission site is located far from the core (i.e., the strong radiation fields have already weakened by the time they reach the distant emitting region), although FSRQ blazars typically have $\text{CD} \gtrsim 1$. However, in the optical spectrum of 4FGL J0132.7–0804 shown in Figure 4 of Peña-Herazo et al. (2021), the emission lines $H\alpha$ and $H\beta$ appear to be very narrow, suggesting that this source is not a broad-line blazar or FSRQ, but rather a BL Lac. Therefore, the low CD of this source may be due to a weaker beaming effect rather than low accretion activity.

Out of the 113 sample sources with good fitting results, 28 are classified as BCUs in the 4FGL catalogue. According to our modelling results, all but two of these BCUs have $\text{CD} < 1$, showing similar emission properties to those of BL Lacs. The remaining two BCUs, for which we obtain $\text{CD} \geq 1$, are 4FGL J0611.1+4325 (with $\text{CD} = 1.4$) and 4FGL J1719.3+1205 (with $\text{CD} = 1.5$).

An analysis of potential correlations between black hole mass and key jet properties, including jet viewing angle, magnetic field strength, energy density ratios, jet power components, synchrotron peak frequency, and CD, for the sources shared with Paliya et al. (2021) reveals no significant trends. This suggests that jet emission in EHSPs is primarily governed by local jet conditions rather than the mass of the central black hole. More-

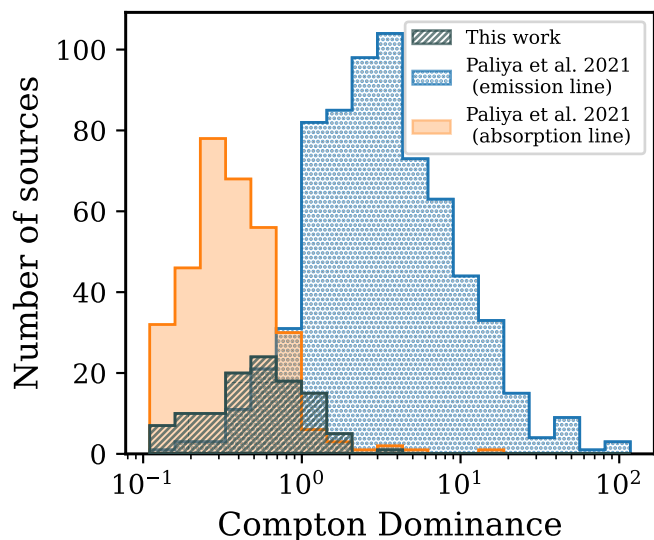


Fig. 9: Comparison of the CD distribution extracted from our results for the 113 sources in the sample with good fits to the results from Paliya et al. (2021) for emission-line and absorption-line blazars.

over, EHSPs consistently show extreme synchrotron peaks and low CD across the full range of black hole masses.

4.2. Host galaxy classification

After modelling all the sources in the sample, we find that the best-fit host galaxy model for 59 sources corresponds to the lenticular galaxy template, while for 54 sources, it corresponds to an elliptical galaxy. Among these, 27 sources match an elliptical galaxy of 13 Gyr, 10 sources match an elliptical galaxy of 5 Gyr, and 17 sources match an elliptical galaxy of 2 Gyr. We note that, although the fitting is done using four different host galaxy templates, it is often difficult to distinguish between the three elliptical galaxy templates, as seen in Figure 4. The best-fit host galaxy results given in Table B.1 correspond to the host galaxy template that yields the lowest χ^2 value, but the difference between the different elliptical galaxy templates can be minimal. For the temperature of the host galaxy, we obtain values ranging from 3.2×10^3 K to 6.4×10^3 K.

In our broadband SED modelling, we use templates for elliptical and lenticular galaxies to estimate the thermal emission from the host galaxy. Figure 10 shows that no significant differences are observed between the two types of galaxies. This supports the conclusion that the emission from the host galaxy has a negligible impact on the blazar’s non-thermal emission. Even in galaxies with high star formation rates, the thermal emission is unlikely to significantly contribute to the high-energy regime, particularly for EHSPs. This is consistent with the findings of Scarpa et al. (2000) and Ghisellini et al. (2011), who argue that the thermal emission from the host galaxy is generally not a significant source of seed photons for the external Compton mechanism. While external Compton on star-forming photons could contribute additional components in some extreme cases, like M82 (Ghisellini et al. 2017), we find that this effect does not substantially alter the SEDs of the majority of EHSPs.

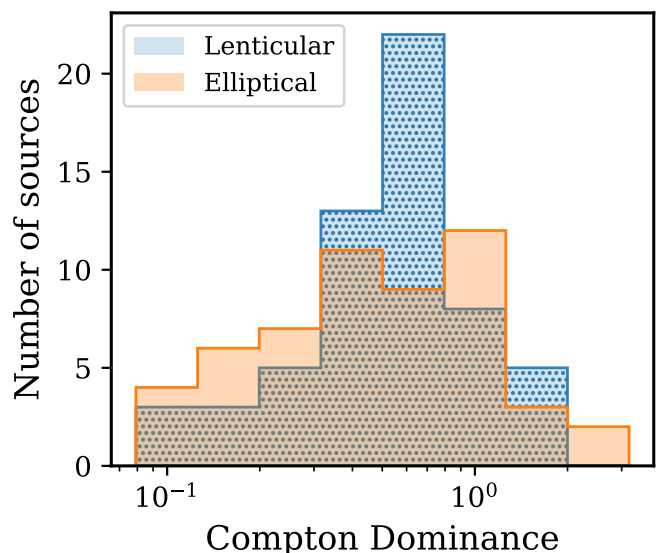


Fig. 10: CD distribution of the resulting lenticular (blue) and elliptical host galaxies (orange) in the sample.

4.3. Energy budget

JetSet modelling also provides an energy report for the resulting best-fit model, including the magnetic and kinetic energy densities, U_B and U_e , respectively. U_B quantifies the energy stored in the magnetic field per unit volume, while U_e represents the energy carried by the population of relativistic electrons, often derived from the modelled electron distribution in the jet. Additional outputs from JetSet include the luminosity of each emission process, i.e., synchrotron and IC, and the jet luminosity associated with radiative mechanisms, electrons, and the magnetic field. The ratio U_B/U_e , representing the energy density of the magnetic field to that of the relativistic electrons, is a critical parameter for understanding the physical conditions and energy balance within blazar jets. This quantity reveals the jet’s magnetisation and the balance between magnetic fields and particle energies in producing the observed radiation. A jet close to equipartition ($U_B/U_e \sim 1$) is thought to be energetically efficient, as such a configuration minimizes energy losses during the acceleration and transport of particles. In the context of EHSPs, studying U_B/U_e helps to probe the mechanisms responsible for their extreme synchrotron peak frequencies, such as efficient particle acceleration and strong magnetic fields. Furthermore, deviations from equipartition can indicate variations in jet dynamics, such as regions of high particle dominance during flaring states or magnetic dominance in steady emission. These characteristics are crucial for modelling the jets and understanding the interplay between synchrotron and inverse Compton processes, as well as the overall energy budget of the system. These energy budget results are given in Table B.2. Figure 11 illustrates the relationship between the magnetic and kinetic energy densities resulting from the SED modelling for the 113 sources in the sample with a good fitting result ($\chi^2/\text{dof} < 1.5$). For comparison, the results for the magnetic and kinetic energy densities from Tavecchio & Ghisellini (2016), Nievas Rosillo et al. (2022), and Zhao et al. (2024) are also shown.

Interestingly, our results suggest a relation between the U_B/U_e ratio and the synchrotron peak frequency, with the least energetic sources having lower values of U_B/U_e , and the most extreme sources located closer to the line $U_B \approx U_e$. To verify

if there is a dependence of the U_B/U_e ratio on the synchrotron peak frequency, we divide our sample into three subsamples with different ranges of $\nu_{\text{sync}}^{\text{peak}}$ values obtained from our SED modelling. The three subsamples have approximately the same number of sources, and their U_B/U_e distributions are shown in Figure 11. We fit each of the three distributions of the U_B/U_e ratio to a Gaussian function, obtaining the following results for the mean and standard deviation: for the distribution of sources with $\nu_{\text{sync}}^{\text{peak}} \leq 6.7 \times 10^{16}$ Hz, $\langle \log(U_B/U_e) \rangle = -1.89$, $\sigma = 1.30$; for the distribution of sources with 6.7×10^{16} Hz $< \nu_{\text{sync}}^{\text{peak}} \leq 4.3 \times 10^{17}$ Hz, $\langle \log(U_B/U_e) \rangle = -1.45$, $\sigma = 1.08$; and for the distribution of sources with $\nu_{\text{sync}}^{\text{peak}} > 4.3 \times 10^{17}$ Hz, $\langle \log(U_B/U_e) \rangle = -0.90$, $\sigma = 1.40$. Therefore, we conclude that the most extreme sources are generally closer to equipartition than the sources with lower synchrotron peak frequencies. This is in agreement with the results obtained by Nievas Rosillo et al. (2022), where most of the sources in their sample, which contains 17 EHSP candidates out of the total 22 sources, were close to equipartition.

However, most sources from the samples of Zhao et al. (2024) and Tavecchio & Ghisellini (2016) are far from equipartition, with the magnetic energy density being much smaller than the electron energy density, clustering mainly around the line $U_B = 10^{-2} \times U_e$. The source sample used by Zhao et al. (2024) contains 348 HSP blazars. Their initial sample was selected by collecting all the blazars classified as HBL in the 4FGL catalogue. Afterwards, they modelled the broadband SED and selected only those blazars with a synchrotron peak frequency of $\nu_{\text{sync}}^{\text{peak}} \geq 10^{15}$ Hz. Among these resulting 348 sources, 42 are also included in our sample. On the other hand, Tavecchio & Ghisellini (2016) selected 45 BL Lac objects, 12 of which were detected in the TeV γ -ray band. Note that sources detected in the TeV band may show biased results since they are typically detected during flaring episodes. These sample selections can help explain the differences in the obtained results, since the source samples from Tavecchio & Ghisellini (2016) and Zhao et al. (2024) also include variable sources. This variability suggests that during certain observations, such sources may be far from equilibrium (e.g., during flares), and in those cases, the electron energy injection could be higher. This would lead to a lower magnetisation, and consequently, to a lower U_B/U_e ratio. In contrast, the sources in our sample are characterised by low variability across various wavelengths, due to the selection criteria applied, and it is expected that they are closer to equipartition.

4.4. The blazar sequence and the role of EHSP blazars

The blazar sequence, a widely used framework in blazar astrophysics, posits an anti-correlation between luminosity and synchrotron peak frequency, with FSRQs typically representing luminous, low synchrotron peak sources, and HSPs and EHSPs occupying the lower-luminosity, high-peak regime (Fosfati et al. 1998; Ghisellini et al. 2017). Our identification of 66 new EHSP candidates reinforces aspects of this model while raising intriguing questions about its universality. The prevalence of EHSPs at the lower-luminosity end aligns with the expected anti-correlation, while their low CD values, as seen in Figure 7, reflect the reduced influence of external photon fields as synchrotron peak frequency increases (Ghisellini et al. 2017).

However, the large number of EHSPs we identify may challenge previous assumptions about this source type. Instrumental sensitivity limits, biased selection criteria, incomplete data coverage, and theoretical models may not have fully captured the diversity of blazars (e.g., Ghisellini 2016; Biteau et al.

2020). If EHSPs are more common than previously thought, the sharp dichotomy between low-luminosity, high-peak blazars and their luminous, low-peak counterparts could soften, suggesting a more continuous distribution. This shift challenges the sequence's traditional boundaries and invites consideration of alternative interpretations. Furthermore, the difficulty of detecting EHSPs at high redshifts due to their lower luminosity introduces a selection bias (e.g., Giommi et al. 2012; Paliya 2015; Ajello et al. 2022), potentially skewing the observed relationship between luminosity and synchrotron peak frequency.

The trends in CD provide additional context. The prevalence of low CD values among EHSPs suggests that synchrotron/SSC processes dominate their emission, consistent with the absence of strong external photon fields (Paliya et al. 2021). This contrasts with the high CD values typically seen in FSRQs, where external Compton scattering plays a significant role (e.g., Sol & Zech 2022). Comparing the CD distribution of EHSPs to other blazar types (see Figure 9) highlights the distinct physical environments and emission mechanisms across the blazar population.

EHSPs, with their extreme synchrotron peaks and low CD, may represent either the natural extension of the blazar sequence or a distinct subclass that deviates from its predictions. Some of the most extreme EHSPs in the sample, particularly those with the highest peak frequencies and $CD \gtrsim 1$, challenge the traditional framework (e.g., Tavecchio et al. 2010). If their underlying jet physics or environmental conditions differ significantly, they could necessitate a revised model that better captures the diversity of the blazar population. The detectability predictions for EHSPs with the CTAO provide an opportunity to test these ideas. Observations of EHSPs at higher redshifts or with unexpected luminosity characteristics could further refine the blazar sequence or point toward its limitations.

These results suggest that while the blazar sequence provides a useful framework, it may oversimplify the diversity of blazars. EHSPs challenge the universality of the sequence, pointing to the need for models that accommodate the complexities of their environments, emission mechanisms, and population statistics (e.g., Biteau et al. 2020; Acciari et al. 2020). This perspective enriches the understanding of blazars and provides a foundation for exploring their classification and evolution in greater depth.

5. Detectability predictions with CTAO

Characterised by spectra extending to extremely high frequencies, EHSPs are generally regarded as promising VHE emitters (e.g., Foffano et al. 2019; Acciari et al. 2020; Zhu et al. 2021). Since the higher-energy component of the SED peaks in the VHE range for many EHSPs, studying these sources at TeV energies ($\sim 10^{26}$ Hz) is essential to understand the acceleration processes occurring in their jets. However, their low fluxes, relatively steady emission, and EBL attenuation at TeV energies make their detection in the VHE band challenging. As a result, only a few EHSPs have been observed above 100 GeV, mostly by the current generation of IACTs: MAGIC, VERITAS, and H.E.S.S. The upcoming Cherenkov Telescope Array Observatory (CTAO; Cherenkov Telescope Array Consortium et al. 2019) will represent the next generation of IACTs. These telescopes detect the faint flashes of Cherenkov light produced by the interaction of the γ rays with the atmosphere and can only operate during the night, resulting in low duty cycles. Consequently, selecting promising targets for VHE detection is important to optimise the observation time of IACTs. Observations by

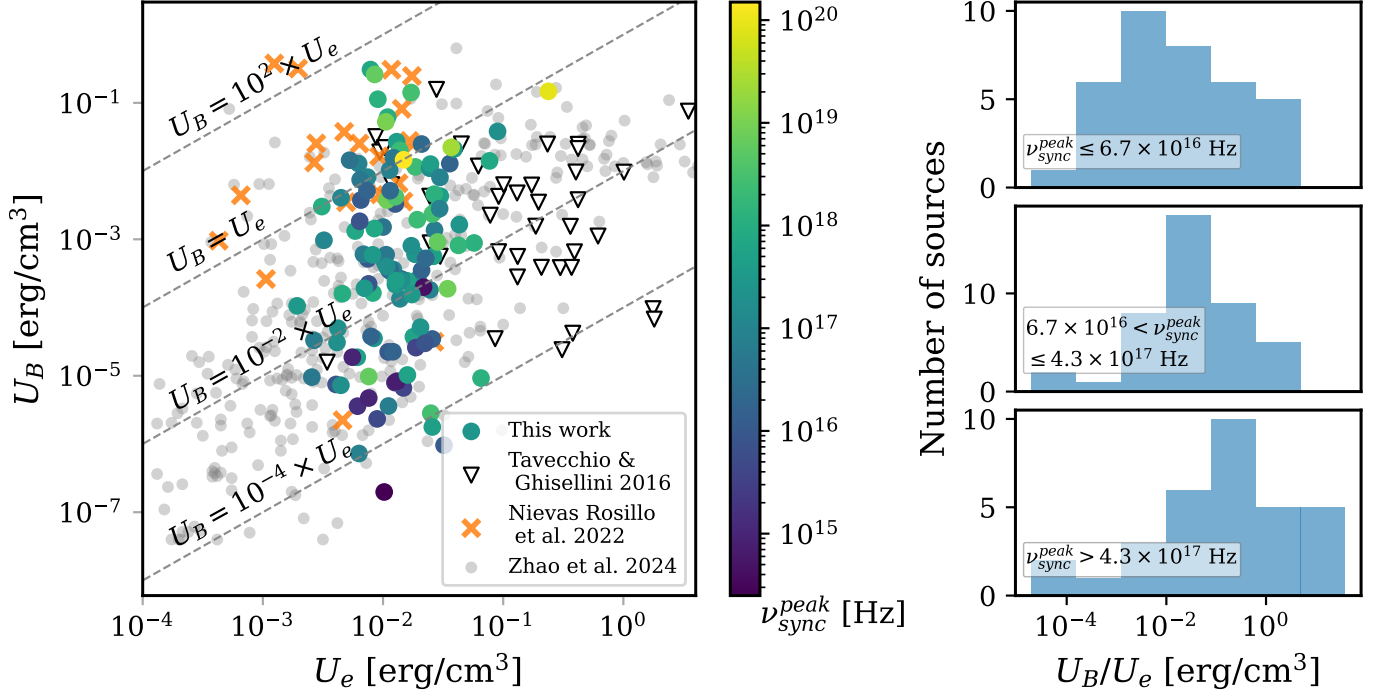


Fig. 11: Left: Magnetic energy density versus kinetic energy density for the 113 sources in the sample with a good fitting result, with colour representing their synchrotron peak frequency. For comparison, the results obtained by Tavecchio & Ghisellini (2016) (as black triangles), Nieves Rosillo et al. (2022) (as orange crosses), and Zhao et al. (2024) (as grey circles) are shown. The dashed grey lines represent the lines for $U_B = 10^2 \times U_e$, $U_B = U_e$ (equipartition), $U_B = 10^{-2} \times U_e$, and $U_B = 10^{-4} \times U_e$. Right: Distribution of the ratio of magnetic energy density to kinetic energy density (U_B/U_e) for three different samples, corresponding to three ranges of synchrotron peak frequency: $\nu_{\text{sync}}^{\text{peak}} \leq 6.7 \times 10^{16}$ Hz (top), 6.7×10^{16} Hz $< \nu_{\text{sync}}^{\text{peak}} \leq 4.3 \times 10^{17}$ Hz (middle), and $\nu_{\text{sync}}^{\text{peak}} > 4.3 \times 10^{17}$ Hz (bottom).

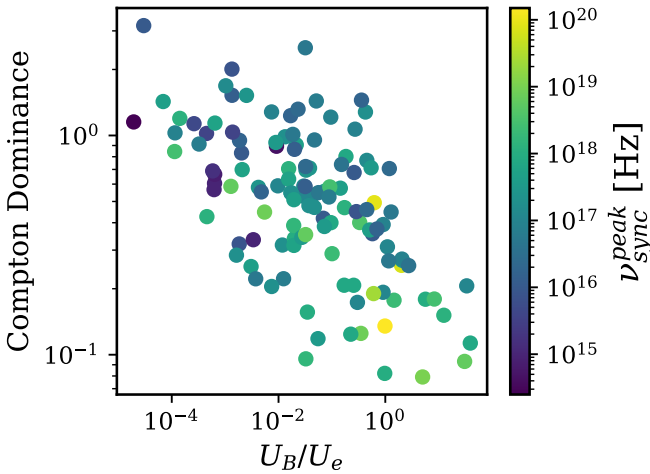


Fig. 12: CD as a function of the ratio between the magnetic and the kinetic energy density.

arrays such as LHAASO or SWGO could also complement these observations for the highest-energy γ -ray emitters.

Using the spectral shape resulting from the SED modelling explained in Section 3, we estimate the expected detection significance of the modelled sources with the future CTAO assuming a total observation time of 20 hours, following the procedure presented in Domínguez et al. (2024a). For this, our best-

fit broadband model is extrapolated to TeV energies, incorporating γ -ray absorption due to EBL interactions using the optical depths from Domínguez et al. (2024b), based on the EBL model by Saldana-Lopez et al. (2021). The significance estimation for each source is done using the CTAO instrument response functions⁵ (IRFs) for the *Alpha Configuration* with an average azimuth angle. These IRFs, produced for three different zenith angles (20 degrees, 40 degrees, and 60 degrees), are available for both the north and south hemisphere CTAO arrays. The CTAO-North IRFs are used for sources with positive declination, while the CTAO-South IRFs are used for sources with negative declination. The zenith angle at which each source is observed is determined by assuming observations around culmination time, and the IRF configuration corresponding to the closest zenith angle is used for the significance estimation. Note that the energy threshold is taken as the energy of the lowest bin of the differential sensitivity curve, meaning that the threshold is higher for larger zenith angle observations and for sources in the southern hemisphere. This is because the CTAO northern array, equipped with larger telescopes, is optimized for greater sensitivity to lower-energy γ -rays, whereas the southern array is designed to detect the highest-energy Cherenkov showers.

Following the procedure by Domínguez et al. (2024a), point-like differential sensitivity curves for a total exposure time of 20 hours are generated by scaling the IRFs corresponding to a 5-hour exposure with gammapy (Deil et al. 2017; Acero et al. 2022). From this analysis, we derive the differential flux, as well

⁵ <https://zenodo.org/records/5499839>

Table 1: Expected detection significance with CTAO and redshift of the 20 sources of the sample that have an expected detection significance $\geq 3\sigma$ with CTAO in 20 hours of observation. For the sources with an expected detection significance $\geq 3\sigma$, but $< 5\sigma$, the time needed to obtain a 5σ detection is also given in the fifth column ($t_{5\sigma}$). The sources are sorted by right ascension (RA) in increasing order. In the redshift reference column, P21 corresponds to Paliya et al. (2021) and G21 to Goldoni (2021).

4FGL Name	CTAO (σ)	Redshift	Redshift reference	$t_{5\sigma}$ [h]
J0013.9–1854	3.9	0.095	P21	34
J0039.1–2219	9.8	0.062	4LAC	–
J0054.7–2455	4.9	0.12	4LAC	21
J0059.3–0152	4.3	0.14	P21	27
J0123.7–2311	5.7	0.4	G21	–
J0336.5–0348	5.0	0.16	4LAC	–
J0357.2–0319	3.4	0.3	3HSP	44
J0536.4–3343	8.3	0.34	4LAC	–
J0558.0–3837	4.5	0.3	P21	24
J0813.7–0356	3.3	0.33	3HSP	47
J0912.9–2102	17.0	0.2	P21	–
J1132.2–4736	3.5	0.23	P21	40
J1256.2–1146	5.5	0.058	P21	–
J1310.2–1158	3.3	0.14	G21	46
J1539.7–1127	4.9	0.22	3HSP	21
J1656.9–2010	5.1	0.46	G21	–
J1841.3+2909	3.6	0.29	G21	39
J1944.4–4523	3.9	0.21	3HSP	34
J2041.9–3735	6.1	0.099	G21	–
J2340.8+8015	6.1	0.27	G21	–

as the number of excess and background events required to generate a 5σ signal within each energy bin. This number of excess events is then scaled linearly with the ratio of the differential fluxes, which is the differential flux in each energy bin for the assumed spectral shape of the source divided by the differential flux derived from the sensitivity curve. As a result, the number of excess events for the considered source is obtained. Finally, the expected detection significance for each source is estimated by applying the equation from Li & Ma (1983) to the obtained number of excess and background events, using the `WStatCountsStatistic` function in `gammapy`.

Out of the 113 blazars in the sample, 9 sources appear to be potential VHE emitters, with an expected detection significance $\geq 5\sigma$ after 20 hours of exposure with CTAO. There are 11 additional sources with an expected detection significance $\geq 3\sigma$ that could be detected with a longer exposure (see Table 1). According to our SED modelling results, of the 20 sources detectable above 3σ , 12 sources have $\nu_{sync}^{peak} \geq 10^{17}$ Hz. Additionally, all these sources are characterised by very low magnetisation, with magnetic field values ranging from 0.0084 to 0.74 Gauss. However, we observe no clear relation between the U_B/U_e ratio and their detectability predictions with the future CTAO, adding to the findings of Nievas Rosillo et al. (2022), who identified the two potential VHE emitters in their sample as having the smallest U_B/U_e ratios.

Notably, the only source in our blazar sample that has already been detected by an IACT (4FGL J0013.9–1854, or SHBL J001355.9–185406) shows an expected detection significance of 3.9σ in our analysis, calculated for 20 hours of CTAO observations. This result aligns well with its previous detection by

H.E.S.S., a less sensitive instrument, which required 41.5 hours of exposure. The source’s steady emission across all wavelengths (H. E. S. S. Collaboration et al. 2013) and the possibility of it undergoing a mild γ -ray flare during the H.E.S.S. observations further highlight its potential as a strong candidate for VHE detection with CTAO.

6. Summary and conclusions

In this work, we conducted a systematic search for EHSPs by reconstructing and modelling the broadband SEDs of 124 blazars selected from the 2BIGB catalogue, further analysing 113 of them with good fits. To build the multi-wavelength SEDs, an analysis of *Swift*-XRT and *Swift*-UVOT data was performed. In addition, the *Fermi*-LAT flux data provided in the 4FGL catalogue were added in the γ -ray band, as well as archival data from the SSDC SED builder service. Integrating multi-wavelength datasets from different epochs and analyses, involving different settings and methodologies, highlights the importance of open science efforts, and the development of standardised multi-wavelength data formats and analyses.

The broadband SEDs were modelled assuming non-flaring states, allowing us to determine key parameters such as synchrotron peak frequency (ν_{sync}^{peak}) and CD. Using a one-zone SSC model, complemented by host galaxy templates, we identified 66 new EHSP candidates, approximately doubling the known population of these rare and intriguing objects. The results revealed that most EHSPs in the sample present low CD values ($CD < 1$), consistent with SSC-dominated emission in environments with weak external photon fields. Host galaxy emission was fitted using templates for lenticular and elliptical galaxies, but no significant differences were observed in the radiative properties of sources hosted by different galaxy types. This suggests that the thermal contribution from the host galaxy has a negligible impact on the high-energy emission.

The analysis of the energy densities in the jet, U_B (magnetic) and U_e (electron), revealed that EHSPs are generally closer to equipartition ($U_B/U_e \sim 1$) compared to less extreme blazars. This indicates that their jets are radiatively efficient, possibly due to finely balanced particle acceleration and magnetic field strengths. A correlation between ν_{sync}^{peak} and U_B/U_e suggests that higher synchrotron peak frequencies are associated with jets closer to energy equilibrium. Our results complement and extend the findings of previous works, such as Nievas Rosillo et al. (2022) and Zhao et al. (2024), while highlighting differences in the relationship between U_B/U_e and detectability. This underscores the importance of sample selection and variability criteria in shaping the inferred physical properties of EHSPs.

Using the modelled SEDs, we calculated detectability predictions for CTAO. Nine sources were identified as strong candidates for VHE γ -ray detection, with expected detection significances above 5σ in 20 hours of observation. An additional 11 sources could be detected at 5σ with slightly longer exposures.

In conclusion, this study demonstrates the value of broadband SED modelling in identifying and characterising EHSPs, providing a better understanding of the extreme physics of their jets. The identification of 66 new candidates not only broadens the population of known EHSPs but also provides critical targets for future observations with CTAO. These sources serve as natural laboratories for exploring particle acceleration, jet dynamics, and the broader blazar sequence. Future multi-wavelength campaigns and deeper VHE observations will be essential to further

refine our understanding of these extraordinary objects and their role within the AGN population.

Acknowledgements. M.L. and J.L.C. acknowledge the support of MCIN project PID2022-138132NB-C42 and grant PRE2020-093502. M.N.R. acknowledges support from the Agencia Estatal de Investigación del Ministerio de Ciencia, Innovación y Universidades (MCIU/AEI) under grant PARTICIPACIÓN DEL IAC EN EL EXPERIMENTO AMS and the European Regional Development Fund (ERDF) with reference PID2022-137810NB-C22/DIO 10.13039/501100011033. A.D. is thankful for the support of Proyecto PID2021-126536OA-I00 funded by MCIN / AEI / 10.13039/501100011033. This research has made use of the CTA instrument response functions provided by the CTA Consortium and Observatory, see <https://www.ctao-observatory.org/science/cta-performance/> (version prod5 v0.1; Cherenkov Telescope Array Observatory and Cherenkov Telescope Array Consortium 2021) for more details. This work made use of data supplied by the UK Swift Science Data Centre at the University of Leicester. Part of this work is based on archival data, software or online services provided by the Space Science Data Center - ASI.

References

- Abdo, A. A., Ackermann, M., Agudo, I., et al. 2010, *ApJ*, 716, 30
- Abdollahi, S., Acero, F., Ackermann, M., et al. 2020, *The Astrophysical Journal Supplement Series*, 247, 33
- Acciari, V. A., Ansoldi, S., Antonelli, L. A., et al. 2020, *ApJS*, 247, 16
- Acero, F., Aguasca-Cabot, A., Buchner, J., et al. 2022, *Gammapy: Python toolbox for gamma-ray astronomy*, If you use this software, please cite it using the metadata from this file.
- Ackermann, M., Ajello, M., Allafort, A., et al. 2011, *ApJ*, 743, 171
- Ajello, M., Angioni, R., Axelsson, M., et al. 2020, *ApJ*, 892, 105
- Ajello, M., Baldini, L., Ballet, J., et al. 2022, *ApJS*, 263, 24
- Ajello, M., Gasparrini, D., Sánchez-Conde, M., et al. 2015, *ApJ*, 800, L27
- Ajello, M., Romani, R. W., Gasparrini, D., et al. 2014, *ApJ*, 780, 73
- Arnaud, K. A. 1996, in *Astronomical Society of the Pacific Conference Series*, Vol. 101, *Astronomical Data Analysis Software and Systems V*, ed. G. H. Jacoby & J. Barnes, 17
- Arsioli, B., Chang, Y. L., & Musiimenta, B. 2020, *MNRAS*, 493, 2438
- Astropy Collaboration, Price-Whelan, A. M., Lim, P. L., et al. 2022, *ApJ*, 935, 167
- Astropy Collaboration, Price-Whelan, A. M., Sipőcz, B. M., et al. 2018, *AJ*, 156, 123
- Astropy Collaboration, Robitaille, T. P., Tollerud, E. J., et al. 2013, *A&A*, 558, A33
- Atwood, W. B., Abdo, A. A., Ackermann, M., et al. 2009, *ApJ*, 697, 1071
- Ballet, J., Bruel, P., Burnett, T. H., Lott, B., & The Fermi-LAT collaboration. 2023, *arXiv e-prints*, [arXiv:2307.12546](https://arxiv.org/abs/2307.12546)
- Beckmann, V., Engels, D., Bade, N., & Wucknitz, O. 2003, *A&A*, 401, 927
- Biteau, J., Prandini, E., Costamante, L., et al. 2020, *Nature Astronomy*, 4, 124
- Blandford, R. & Eichler, D. 1987, *Phys. Rep.*, 154, 1
- Bonnoli, G., Tavecchio, F., Ghisellini, G., & Sbarrato, T. 2015, *MNRAS*, 451, 611
- Böttcher, M., Reimer, A., Sweeney, K., & Prakash, A. 2013, *ApJ*, 768, 54
- Burrows, D. N., Hill, J. E., Nousek, J. A., et al. 2005, *Space Sci. Rev.*, 120, 165
- Celotti, A. & Ghisellini, G. 2008, *MNRAS*, 385, 283
- Chang, Y. L., Arsioli, B., Giommi, P., Padovani, P., & Brandt, C. H. 2019, *A&A*, 632, A77
- Cherenkov Telescope Array Consortium, Acharya, B. S., Agudo, I., et al. 2019, *Science with the Cherenkov Telescope Array*
- Cherenkov Telescope Array Observatory and Cherenkov Telescope Array Consortium. 2021, *CTAO Instrument Response Functions - prod5 version v0.1*
- Combes, F. 2021, *Active Galactic Nuclei: Fueling and Feedback*
- Deil, C., Zanin, R., Lefaucheur, J., et al. 2017, in *International Cosmic Ray Conference*, Vol. 301, 35th International Cosmic Ray Conference (ICRC2017), 766
- Domínguez, A. & Ajello, M. 2015, *ApJ*, 813, L34
- Domínguez, A., Láinez, M., Paliya, V. S., et al. 2024a, *MNRAS*, 527, 4763
- Domínguez, A., Østergaard Kirkeberg, P., Wojtak, R., et al. 2024b, *MNRAS*, 527, 4632
- Domínguez, A., Wojtak, R., Finke, J., et al. 2019, *ApJ*, 885, 137
- Evans, P. A., Beardmore, A. P., Page, K. L., et al. 2009, *MNRAS*, 397, 1177
- Evans, P. A., Beardmore, A. P., Page, K. L., et al. 2007, *A&A*, 469, 379
- Falomo, R., Pian, E., & Treves, A. 2014, *A&A Rev.*, 22, 73
- Finke, J. D., Dermer, C. D., & Böttcher, M. 2008, *ApJ*, 686, 181
- Foffano, L., Prandini, E., Franceschini, A., & Paiano, S. 2019, *MNRAS*, 486, 1741
- Fossati, G., Maraschi, L., Celotti, A., Comastri, A., & Ghisellini, G. 1998, *MNRAS*, 299, 433
- Ghisellini, G. 2016, *Galaxies*, 4, 36
- Ghisellini, G., Righi, C., Costamante, L., & Tavecchio, F. 2017, *Monthly Notices of the Royal Astronomical Society*, 469, 255
- Ghisellini, G., Righi, C., Costamante, L., & Tavecchio, F. 2017, *MNRAS*, 469, 255
- Ghisellini, G., Tavecchio, F., Foschini, L., & Ghirlanda, G. 2011, *MNRAS*, 414, 2674
- Giommi, P., Padovani, P., Polenta, G., et al. 2012, *MNRAS*, 420, 2899
- Goldoni, P. 2021, *Review of redshift values of bright AGNs with hard spectra in 4LAC catalog*
- Gréaux, L., Biteau, J., Hassan, T., et al. 2023, *arXiv e-prints*, [arXiv:2304.00835](https://arxiv.org/abs/2304.00835)
- Gréaux, L., Biteau, J., & Nieves Rosillo, M. 2024, *ApJ*, 975, L18
- H. E. S. S. Collaboration, Abramowski, A., Acero, F., et al. 2013, *A&A*, 554, A72
- Kirk, J. G., Rieger, F. M., & Mastichiadis, A. 1998, *A&A*, 333, 452
- Li, T. P. & Ma, Y. Q. 1983, *ApJ*, 272, 317
- Liu, R.-Y., Rieger, F. M., & Aharonian, F. A. 2017, *ApJ*, 842, 39
- MAGIC Collaboration, Acciari, V. A., Ansoldi, S., et al. 2021, *A&A*, 655, A89
- MAGIC Collaboration, Acciari, V. A., Ansoldi, S., et al. 2020, *A&A*, 637, A86
- Mannheim, K. & Biermann, P. L. 1992, *A&A*, 253, L21
- Maraschi, L., Ghisellini, G., & Celotti, A. 1992, *ApJ*, 397, L5
- Marcha, M. J. M., Browne, I. W. A., Impey, C. D., & Smith, P. S. 1996, *MNRAS*, 281, 425
- Marscher, A. P., Jorstad, S. G., D’Arcangelo, F. D., et al. 2008, *Nature*, 452, 966
- Marschern, A. P. 2010, in *Lecture Notes in Physics*, Berlin Springer Verlag, ed. T. Belloni, Vol. 794, 173
- Mücke, A., Protheroe, R. J., Engel, R., Rachen, J. P., & Stanev, T. 2003, *Astroparticle Physics*, 18, 593
- Nieves Rosillo, M., Domínguez, A., Chiaro, G., et al. 2022, *MNRAS*, 512, 137
- Padovani, P. 2007, *Astrophysics and Space Science*, 309, 63–71
- Padovani, P. 2017, *Frontiers in Astronomy and Space Sciences*, 4, 35
- Padovani, P., Boccardi, B., Falomo, R., & Giommi, P. 2022, *MNRAS*, 511, 4697
- Padovani, P. & Giommi, P. 1995, *ApJ*, 444, 567
- Paliya, V. S. 2015, *ApJ*, 804, 74
- Paliya, V. S., Domínguez, A., Ajello, M., Franckowiak, A., & Hartmann, D. 2019, *ApJ*, 882, L3
- Paliya, V. S., Domínguez, A., Ajello, M., Olmo-García, A., & Hartmann, D. 2021, *ApJS*, 253, 46
- Paliya, V. S., Zhang, H., Böttcher, M., et al. 2018, *ApJ*, 863, 98
- Peña-Herazo, H. A., Paggi, A., García-Pérez, A., et al. 2021, *AJ*, 162, 177
- Polletta, M., Tajer, M., Maraschi, L., et al. 2007, *ApJ*, 663, 81
- Roming, P. W. A., Kennedy, T. E., Mason, K. O., et al. 2005, *Space Sci. Rev.*, 120, 95
- Saldana-Lopez, A., Domínguez, A., Pérez-González, P. G., et al. 2021, *MNRAS*, 507, 5144
- Scargle, J. D., Norris, J. P., Jackson, B., & Chiang, J. 2013, *ApJ*, 764, 167
- Scarpa, R., Urry, C. M., Falomo, R., Pesce, J. E., & Treves, A. 2000, *ApJ*, 532, 740
- Sikora, M., Begelman, M. C., & Rees, M. J. 1994, *ApJ*, 421, 153
- Sironi, L. & Spitkovsky, A. 2014, *ApJ*, 783, L21
- Sol, H. & Zech, A. 2022, *Galaxies*, 10, 105
- Tavecchio, F. & Ghisellini, G. 2016, *MNRAS*, 456, 2374
- Tavecchio, F., Ghisellini, G., Ghirlanda, G., Foschini, L., & Maraschi, L. 2010, *MNRAS*, 401, 1570
- Tavecchio, F., Landoni, M., Sironi, L., & Coppi, P. 2020, *MNRAS*, 498, 599
- Tavecchio, F., Maraschi, L., & Ghisellini, G. 1998, *ApJ*, 509, 608
- Tramacere, A. 2020, *JetSeT: Numerical modeling and SED fitting tool for relativistic jets*, *Astrophysics Source Code Library*, record ascl:2009.001
- Tramacere, A., Giommi, P., Perri, M., Verrecchia, F., & Tosti, G. 2009, *A&A*, 501, 879
- Tramacere, A., Massaro, E., & Taylor, A. M. 2011, *ApJ*, 739, 66
- Urry, C. M. 1996, in *Astronomical Society of the Pacific Conference Series*, Vol. 110, *Blazar Continuum Variability*, ed. H. R. Miller, J. R. Webb, & J. C. Noble, 391
- Urry, C. M. & Padovani, P. 1995, *PASP*, 107, 803
- Urry, C. M., Scarpa, R., O’Dowd, M., et al. 2000, *ApJ*, 532, 816
- van den Berg, J. P., Böttcher, M., Domínguez, A., & López-Moya, M. 2019, *ApJ*, 874, 47
- Zhao, X. Z., Yang, H. Y., Zheng, Y. G., & Kang, S. J. 2024, *ApJ*, 967, 104
- Zhu, K. R., Kang, S. J., Zhou, R. X., & Zheng, Y. G. 2021, *ApJ*, 916, 93

Appendix A: Broadband SEDs and best-fit model of the sample sources

This section presents the broadband SEDs used to model the 124 sources in our sample, along with the best-fit SSC model.

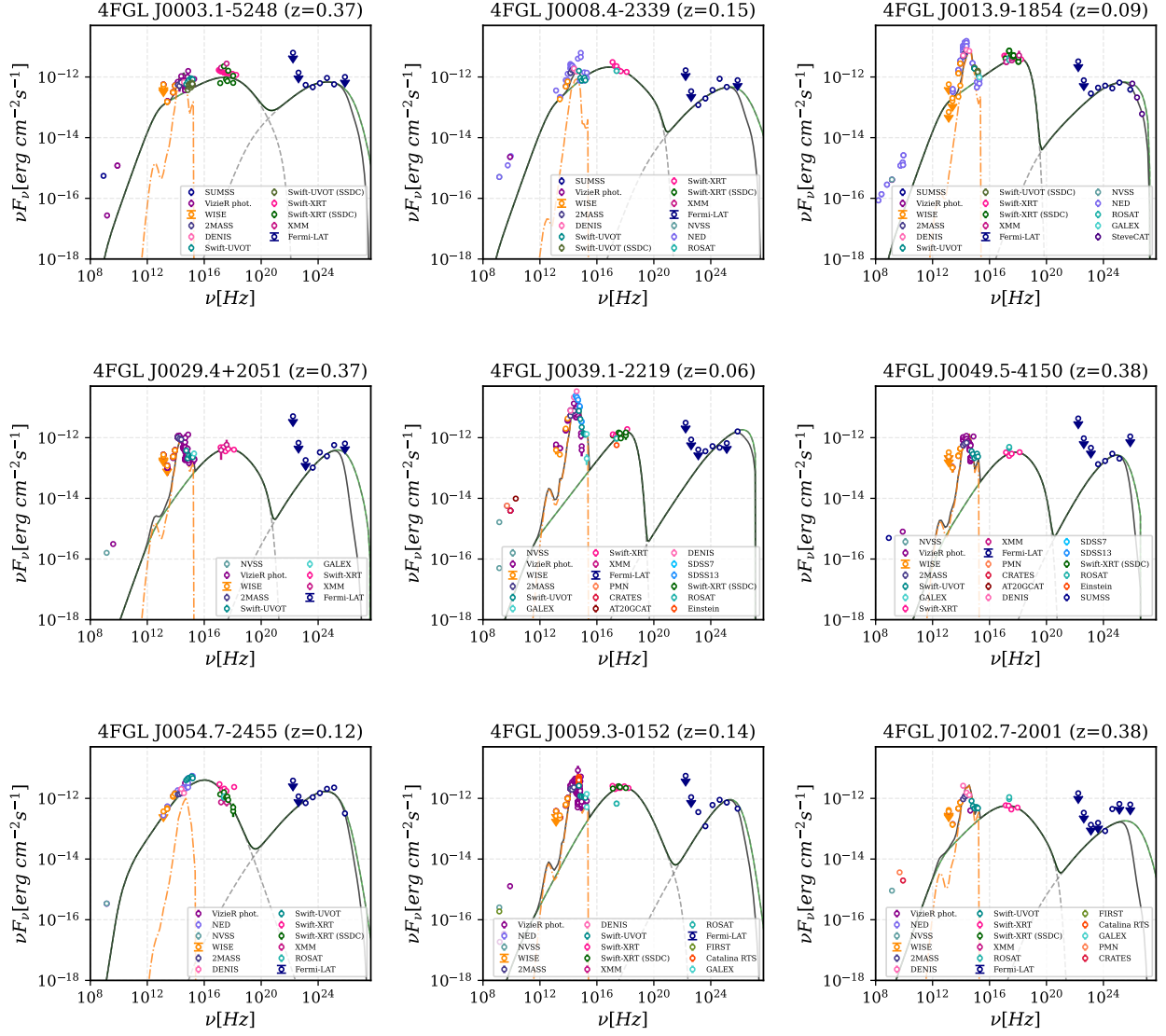


Fig. A.1: The multi-wavelength SEDs of the 124 selected sources are presented with their best-fit models. The fluxes used to reconstruct the SEDs are shown as coloured points. The synchrotron and SSC emission from the best-fit model is represented by a dashed gray line, while the host galaxy emission (based on the best-fit host galaxy model given in Table B.1 for each source) is shown in orange. The total intrinsic emission, summing all components, is represented by a solid green line, and the observed emission, after accounting for EBL absorption, is shown with a solid black line. These SEDs are reconstructed using archival data from the SSDC SED builder service, along with data from *Swift*-XRT, *Swift*-UVOT, *Fermi*-LAT, and the SteveCAT catalogue.

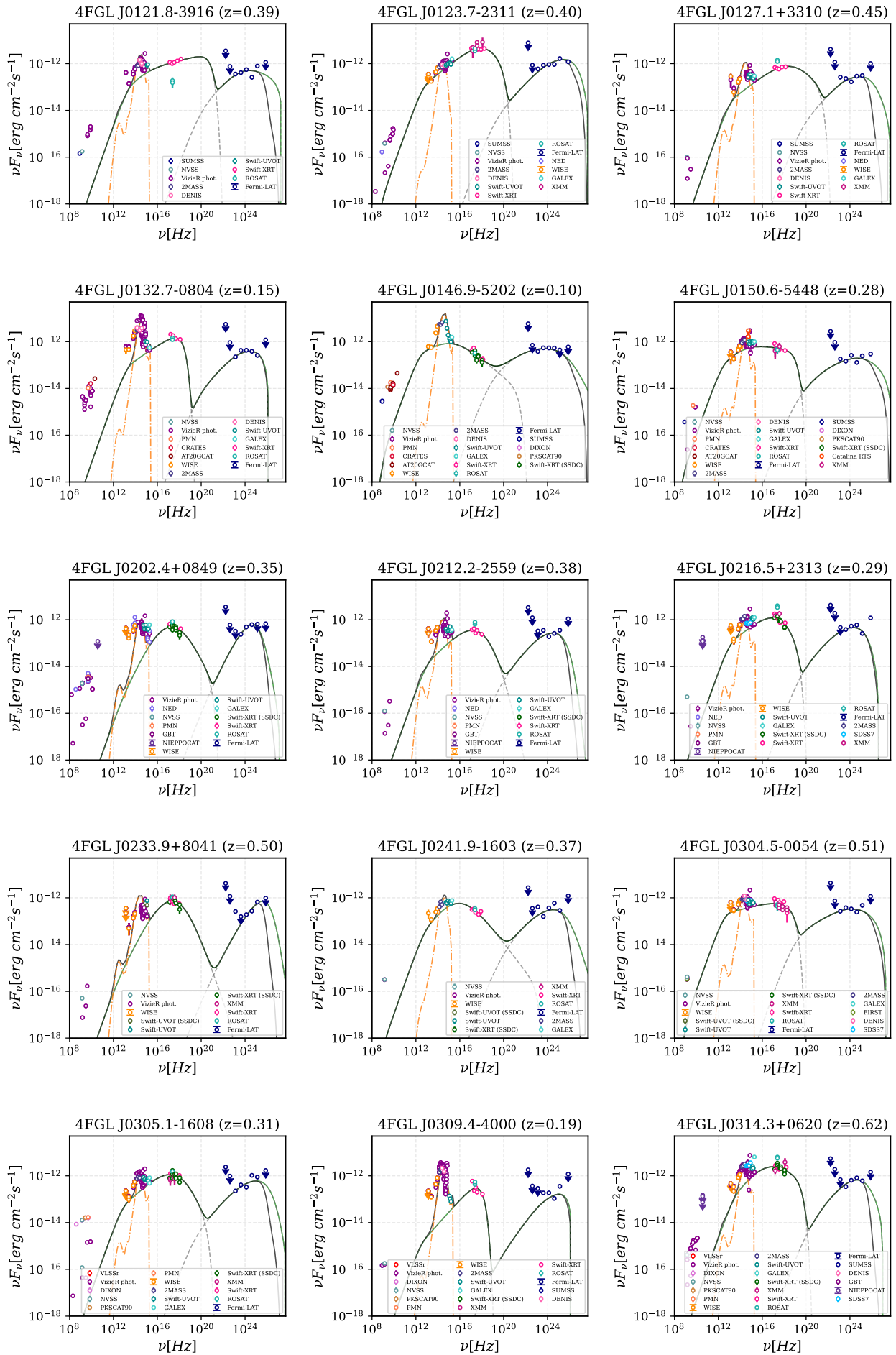


Fig. A.1: continued

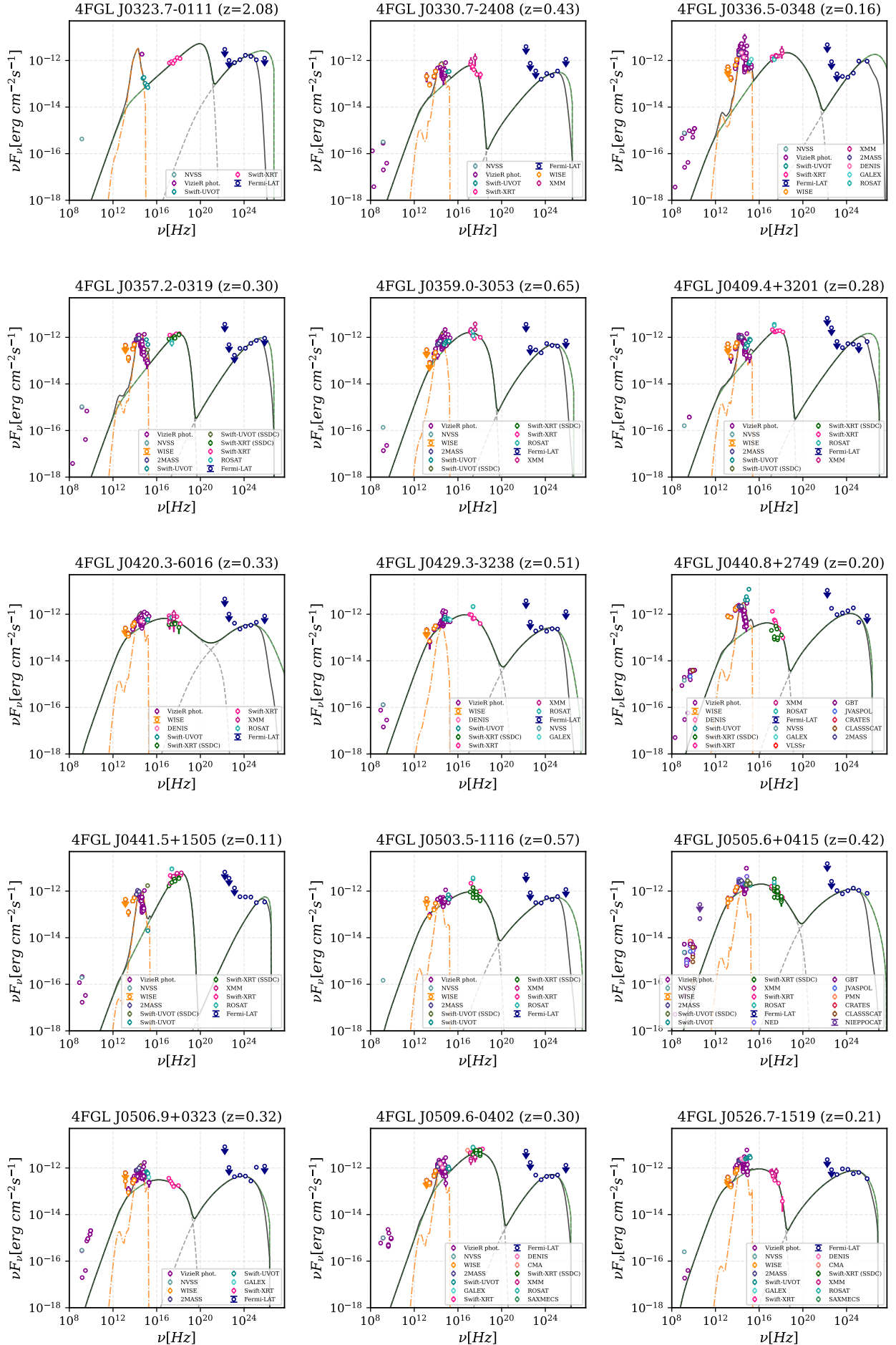
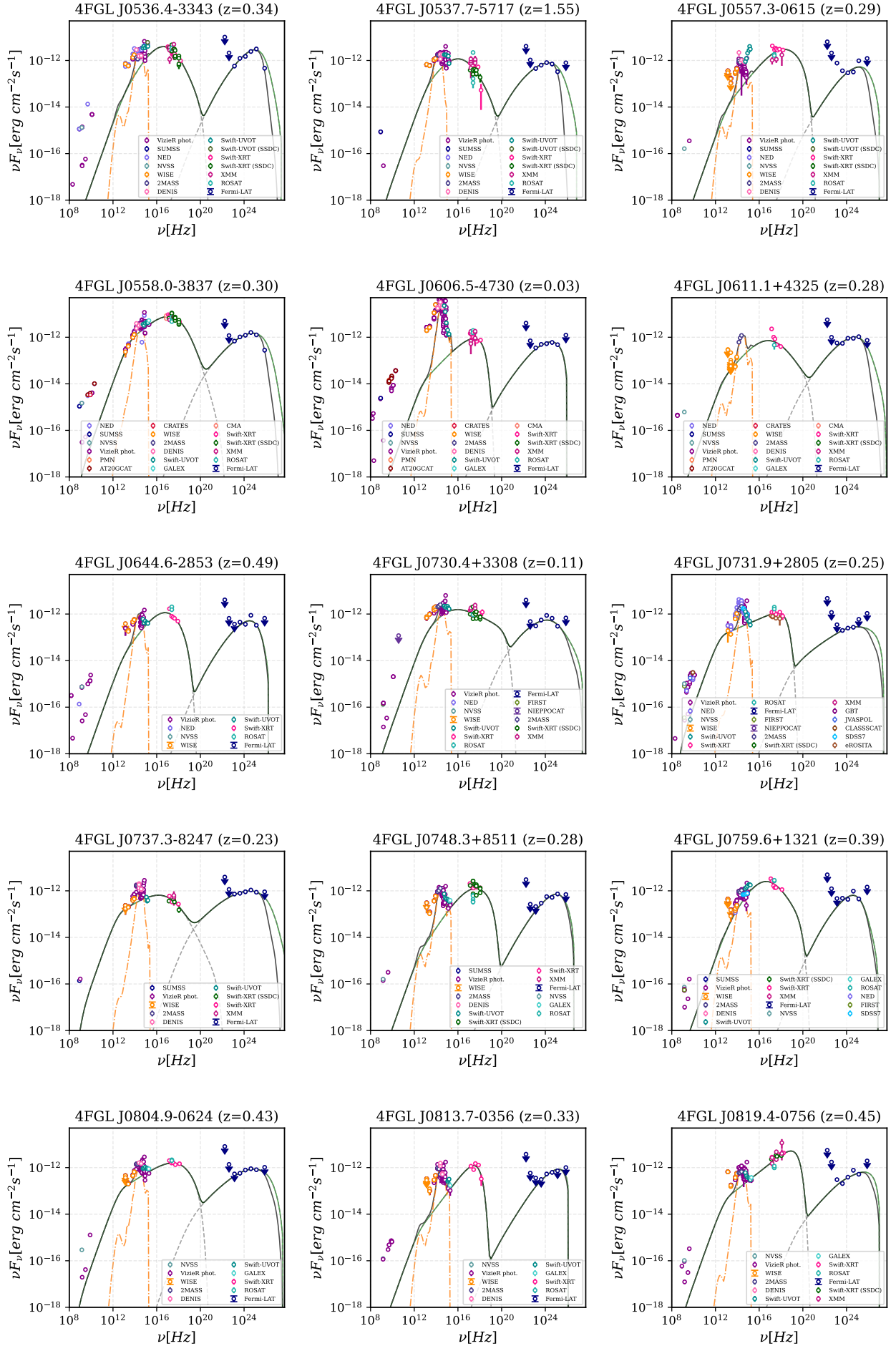


Fig. A.1: *continued*



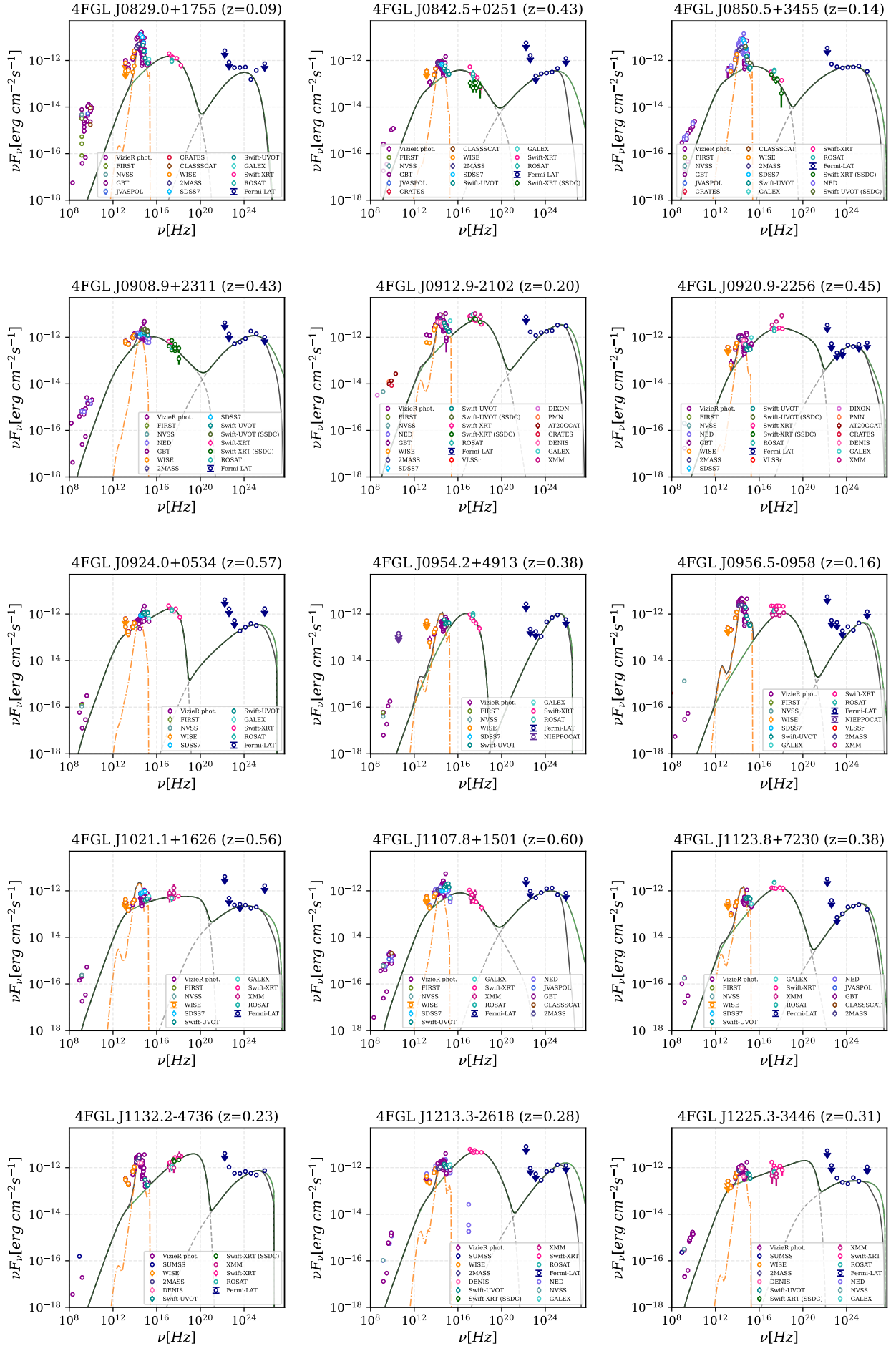


Fig. A.1: continued

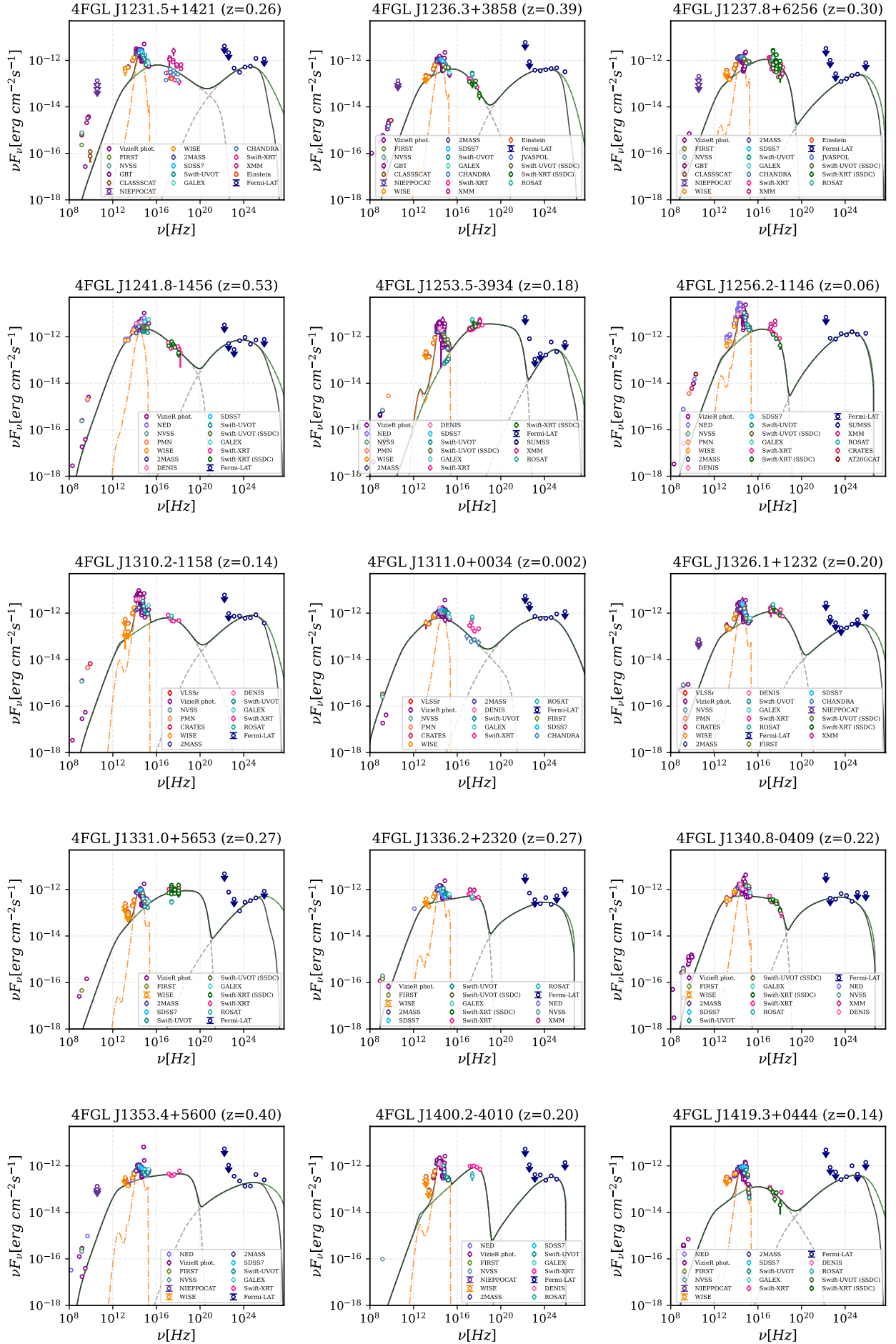


Fig. A.1: continued

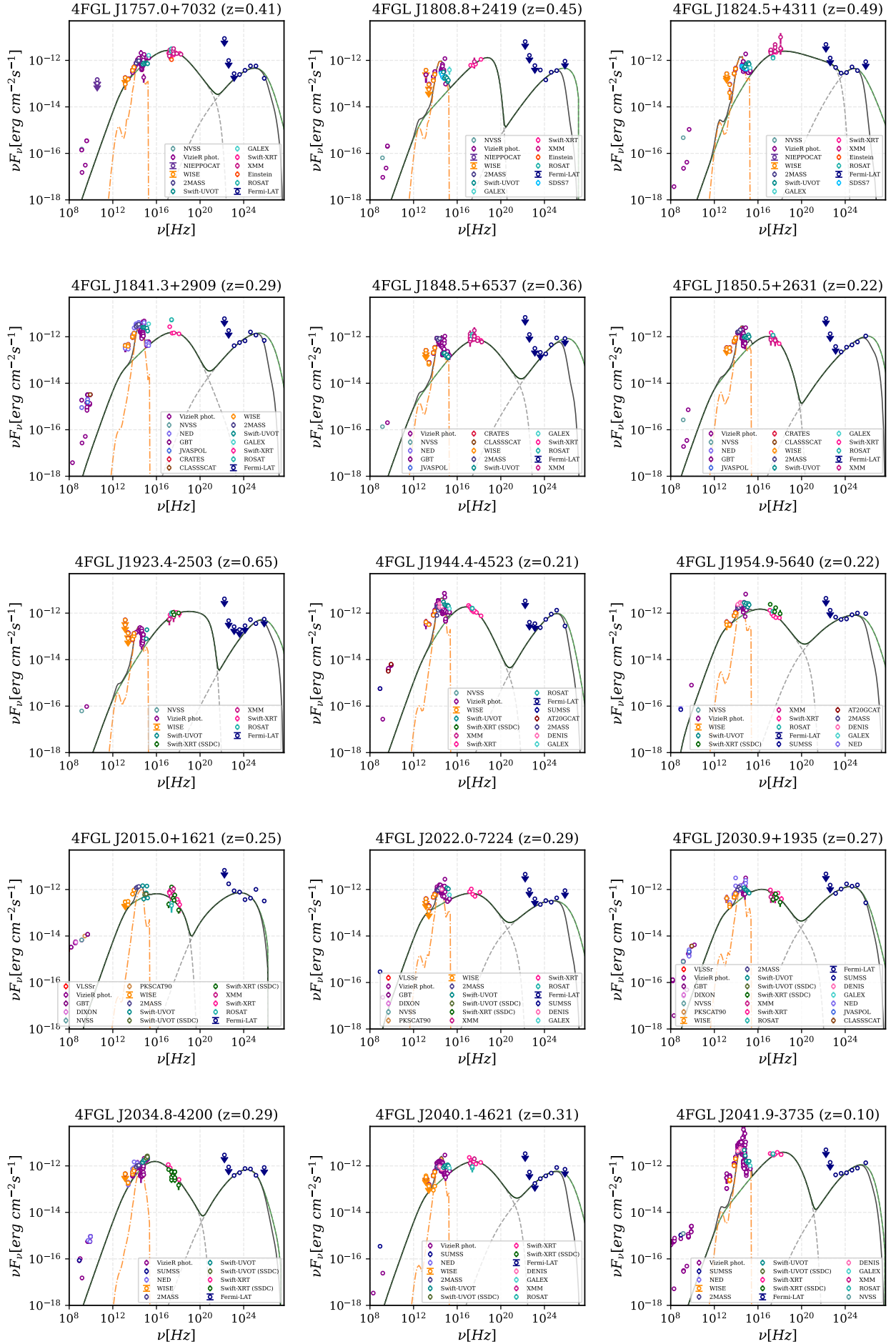
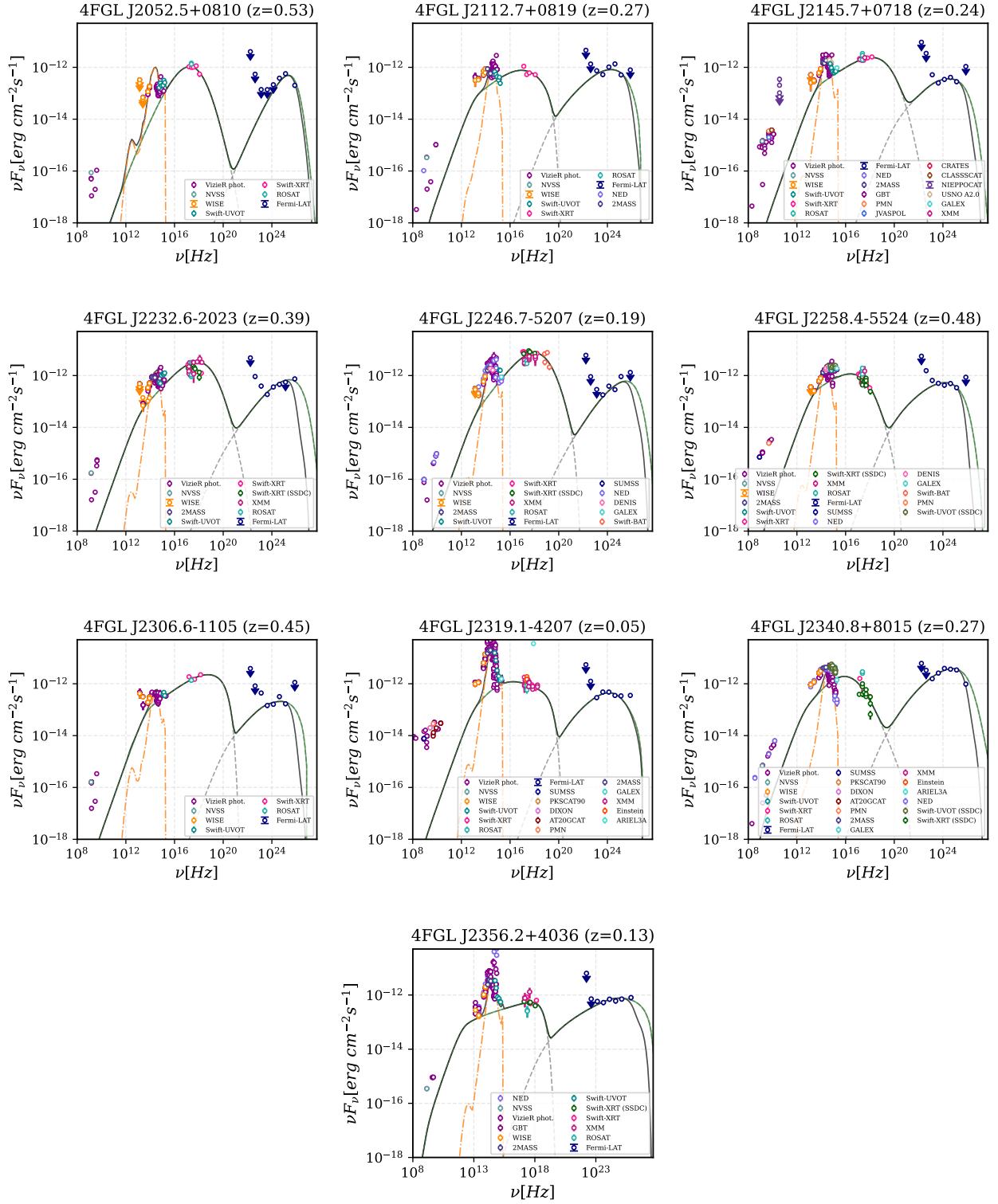


Fig. A.1: *continued*


Fig. A.1: *continued*

Appendix B: Best-fit parameters and energetic report of the sample sources

This section provides the resulting best-fit parameters and energetic report of the sample sources. Table B.1 shows the best-fit parameters obtained from the SED modelling carried out for the 124 sources of the sample using a one-zone SSC model. Table B.2 gives the ν_{sync}^{peak} and CD results, as well as the luminosity of each emitting component and the luminosity carried by the jet for the radiative components, electrons, and magnetic fields.

Table B.1: Best-fit parameters obtained from the broadband SED modelling, including the magnetic field strength B , the jet viewing angle θ , the maximum Lorentz factor γ_{max} , the break Lorentz γ_{break} , the low energy and high energy spectral indices p_1 and p_2 , the electron density N , the best-fitting host galaxy model and the resulting temperature of the host galaxy T_{host} , and the χ^2 used to select sources with a good fitting result. The values of the radius of the emitting region R , the distance from the SMBH R_H and the bulk Lorentz factor Γ are fixed to $R = 10^{16}$ cm, $R_H = 2 \times 10^{18}$ cm, $\Gamma = 20$.

4FGL Name	B [G]	θ [deg]	γ_{max}	γ_{break}	p_1	p_2	N [cm ⁻³]	Host Galaxy	T_{host} [$\times 10^3$ K]	χ^2
J0003.1–5248	0.12	5.4	1.8×10^7	1.3×10^6	2.4	2.9	2.4×10^5	S0	4.3	0.80
J0008.4–2339	0.029	0.017	6.8×10^6	1.7×10^5	2.0	2.1	1.0×10^3	EII13	4.7	0.68
J0013.9–1854	0.063	3.0	9.7×10^5	2.1×10^7	2.3	9.7	1.8×10^4	EII13	4.5	0.72
J0029.4+2051	0.12	5.6	7.2×10^6	5.4×10^5	1.6	3.1	1.2×10^2	S0	3.3	0.55
J0039.1–2219	0.015	7.0	3.0×10^6	1.0×10^2	1.6	0.18	3.5×10^2	S0	4.4	1.0
J0049.5–4150	0.60	11.0	3.3×10^6	8.3×10^5	1.4	4.6	53.0	S0	4.3	0.30
J0054.7–2455	0.11	3.0	4.6×10^8	7.7×10^4	1.5	4.3	48.0	EII2	6.0	0.45
J0059.3–0152	0.26	8.1	2.7×10^7	7.0×10^5	1.2	4.6	1.4	S0	4.7	1.2
J0102.7–2001	0.035	1.1	7.9×10^6	4.4×10^5	2.0	2.8	9.3×10^2	S0	4.3	0.87
J0121.8–3916	0.92	6.0	5.1×10^6	5.0×10^3	1.8	1.0	1.7×10^3	S0	4.4	2.0
J0123.7–2311	0.064	3.4	3.7×10^6	3.4×10^6	2.2	5.5	1.4×10^4	EII5	5.8	0.38
J0127.1+3310	0.54	5.9	1.1×10^7	8.2×10^5	2.3	1.9	4.9×10^4	S0	4.6	0.67
J0132.7–0804	0.82	8.0	3.4×10^5	8.0×10^2	1.6	0.80	7.9×10^2	EII13	4.7	0.41
J0146.9–5202	0.014	1.0	2.6×10^7	3.1×10^4	2.3	1.4	1.0×10^5	EII13	4.5	0.17
J0150.6–5448	0.014	5.3×10^{-3}	2.0×10^6	8.6×10^3	1.8	1.4	5.0×10^2	S0	5.3	1.2
J0202.4+0849	0.98	12.0	7.5×10^6	1.5×10^5	0.70	4.2	0.10	S0	4.2	0.13
J0212.2–2559	0.53	7.0	8.1×10^7	6.4×10^5	2.0	5.2	1.0×10^4	S0	4.3	0.81
J0216.5+2313	0.51	7.5	9.3×10^5	6.9×10^5	2.2	6.0	2.2×10^4	S0	5.3	1.4
J0233.9+8041	0.081	3.9	9.8×10^7	3.8×10^5	0.92	4.8	0.10	S0	4.7	1.2
J0241.9–1603	0.075	2.0	9.2×10^7	3.5×10^4	1.6	2.6	1.2×10^2	EII2	5.6	1.2
J0304.5–0054	0.058	3.6	1.4×10^6	4.1×10^6	2.8	4.7	2.3×10^6	S0	4.8	0.83
J0305.1–1608	0.11	3.0	4.8×10^6	5.4×10^5	2.1	3.5	9.4×10^3	S0	3.2	0.79
J0309.4–4000	0.23	9.0	5.2×10^5	2.0×10^6	2.0	1.1×10^{-6}	3.5×10^3	EII13	4.9	1.6
J0314.3+0620	0.57	3.0	9.1×10^5	4.0×10^4	1.7	2.1	2.1×10^2	S0	5.1	0.57
J0323.7–0111	1.9	7.7	4.7×10^6	1.1×10^3	1.6	0.61	3.6×10^3	EII2	5.7	0.39
J0330.7–2408	0.095	3.3	2.9×10^5	2.0×10^6	2.1	0.80	9.8×10^3	S0	4.5	0.56
J0336.5–0348	8.4×10^{-3}	3.0	5.6×10^7	4.8×10^6	1.6	4.0	46.0	S0	4.8	0.70
J0357.2–0319	0.15	7.0	1.1×10^6	2.0×10^6	1.8	0.40	1.1×10^3	S0	5.3	0.44
J0359.0–3053	0.45	3.4	5.0×10^5	2.4×10^5	1.8	4.4	3.1×10^2	EII2	5.2	0.66
J0409.4+3201	0.031	2.9	8.8×10^5	2.0×10^6	1.9	0.40	9.7×10^2	S0	5.3	0.50
J0420.3–6016	0.12	3.0	2.5×10^7	1.2×10^5	2.2	1.7	2.8×10^4	S0	5.5	0.55
J0429.3–3238	0.43	3.5	1.9×10^6	2.3×10^5	2.1	4.4	6.1×10^3	EII2	6.2	0.38
J0440.8+2749	0.22	7.0	5.0×10^5	3.4×10^5	2.2	2.8	1.0×10^5	S0	4.9	3.3
J0441.5+1505	0.21	10.0	1.2×10^6	1.0×10^7	1.1	1.0	0.24	EII13	4.6	3.0
J0503.5–1116	0.093	1.7	1.4×10^6	1.0×10^6	2.3	5.5	3.5×10^4	S0	4.9	0.26
J0505.6+0415	0.095	1.0	1.8×10^6	1.1×10^5	2.2	2.6	3.6×10^4	S0	4.5	1.2
J0506.9+0323	0.57	7.0	7.7×10^5	3.6×10^4	2.1	1.7	3.0×10^4	S0	5.4	1.1
J0509.6–0402	2.8	7.4	7.7×10^5	4.4×10^5	1.9	4.5	7.0×10^2	S0	4.1	0.73
J0526.7–1519	0.024	2.4	4.8×10^5	1.1×10^5	2.1	2.1	1.0×10^4	EII13	5.0	1.1
J0536.4–3343	0.20	3.0	2.0×10^6	8.8×10^4	1.1	4.5	0.92	S0	4.2	0.40
J0537.7–5717	0.29	1.0	8.7×10^5	4.0×10^4	1.5	3.7	89.0	EII5	4.7	0.33
J0557.3–0615	0.71	6.9	2.7×10^6	1.0×10^6	1.8	4.1	3.1×10^2	S0	5.3	1.5
J0558.0–3837	0.32	2.2	9.9×10^6	3.4×10^5	2.1	4.6	4.7×10^3	EII2	5.3	0.067
J0606.5–4730	0.73	12.0	5.1×10^5	8.3×10^5	2.0	3.0	8.3×10^3	EII13	5.5	0.51
J0611.1+4325	0.19	5.2	5.8×10^6	1.6×10^5	1.8	2.7	1.4×10^3	S0	5.3	0.89
J0644.6–2853	0.63	9.0	6.4×10^5	3.6×10^5	1.6	7.0	68.0	EII13	4.7	0.72
J0730.4+3308	0.31	5.3	3.9×10^6	8.7×10^3	1.1	2.4	4.8	S0	4.6	0.49
J0731.9+2805	0.022	1.9	1.0×10^6	6.1×10^8	2.6	1.0	2.7×10^5	EII5	5.1	0.39
J0737.3–8247	0.029	2.0	2.5×10^7	3.1×10^5	2.4	2.7	2.5×10^5	EII5	5.1	0.41
J0748.3+8511	0.33	10.0	1.6×10^6	8.0×10^5	1.5	4.6	60.0	S0	5.3	0.97
J0759.6+1321	0.60	6.9	1.6×10^6	5.2×10^4	0.95	3.8	0.23	S0	4.4	0.72
J0804.9–0624	0.074	4.1	3.3×10^6	3.3×10^6	2.4	6.5	1.0×10^5	S0	4.5	0.19
J0813.7–0356	0.20	9.8	5.4×10^5	1.9×10^7	1.8	2.2×10^{-5}	6.3×10^2	S0	5.5	0.65
J0819.4–0756	0.31	6.9	2.0×10^6	1.0×10^5	2.3	4.4×10^{-5}	2.4×10^4	EII13	4.6	0.90
J0829.0+1755	3.0	12.0	2.7×10^6	5.7×10^5	2.0	8.0	2.5×10^3	EII13	4.5	1.8
J0842.5+0251	0.024	0.064	8.6×10^6	2.0×10^5	2.1	2.9	1.0×10^4	EII5	5.9	1.1
J0850.5+3455	0.013	1.2	1.5×10^6	1.2×10^5	2.2	2.5	3.0×10^4	EII13	4.7	0.58
J0908.9+2311	7.7×10^{-3}	0.012	1.4×10^7	4.6×10^4	1.5	2.6	36.0	EII2	5.9	0.49
J0912.9–2102	0.079	4.4	3.0×10^8	3.5×10^6	2.0	8.0	3.2×10^3	S0	3.8	1.1
J0920.9–2256	1.2	10.0	1.2×10^7	1.1×10^5	1.6	1.9	1.1×10^2	EII13	4.6	0.45

Continued on next page

Table B.1: *continued*

4FGL Name	B [G]	θ [deg]	γ_{max}	γ_{break}	p_1	p_2	N [cm ⁻³]	Host Galaxy	T_{host} [$\times 10^3$ K]	χ^2
J0924.0+0534	0.028	2.0	5.7×10^5	4.3×10^6	2.4	2.5	3.1×10^4	EII2	6.4	0.38
J0954.2+4913	0.081	6.2	5.7×10^5	3.4×10^5	0.42	7.5	6.0×10^{-4}	S0	4.3	0.37
J0956.5-0958	0.14	10.0	3.2×10^7	3.4×10^6	1.4	6.4	15.0	S0	4.8	1.0
J1021.1+1626	0.33	7.0	5.4×10^6	4.2×10^4	2.5	0.54	2.3×10^5	S0	4.9	0.37
J1107.8+1501	0.094	1.9	4.5×10^7	1.1×10^5	2.1	2.7	1.4×10^4	EII2	5.0	0.58
J1123.8+7230	0.19	7.0	1.5×10^8	2.3×10^6	1.8	7.0	2.0×10^2	S0	4.3	0.29
J1132.2-4736	0.75	12.0	4.4×10^6	7.2×10^5	2.0	0.87	6.3×10^3	EIII3	5.0	1.5
J1213.3-2618	0.052	1.4	8.9×10^6	1.0×10^6	1.8	4.5	1.4×10^2	S0	5.2	2.0×10^6
J1225.3-3446	0.61	8.2	8.9×10^6	5.5×10^6	2.7	3.5×10^{-5}	1.1×10^6	EIII3	5.4	0.55
J1231.5+1421	0.079	3.0	3.2×10^7	3.3×10^4	1.8	2.0	8.0×10^2	EII5	5.2	2.6
J1236.3+3858	0.025	7.7×10^{-3}	6.2×10^6	1.1×10^5	2.3	2.9	6.2×10^4	EIII3	4.4	1.5
J1237.8+6256	0.015	0.50	1.4×10^6	3.3×10^5	2.2	2.5	2.9×10^3	S0	5.3	0.32
J1241.8-1456	0.022	2.9×10^{-4}	4.4×10^6	7.3×10^3	0.64	3.3	0.13	EII2	6.3	1.1
J1253.5-3934	1.2	9.0	1.7×10^7	7.5×10^4	0.94	2.3	0.11	S0	4.8	0.72
J1256.2-1146	0.095	5.0	5.0×10^5	1.0×10^5	1.9	2.2	2.4×10^3	S0	4.3	0.75
J1310.2-1158	0.068	4.6	7.5×10^7	5.8×10^5	2.3	2.7	9.5×10^4	S0	4.7	0.59
J1311.0+0034	2.2×10^{-3}	5.0	6.7×10^7	4.5×10^4	1.7	2.3	3.4×10^2	EII2	5.4	0.77
J1326.1+1232	0.014	0.72	8.3×10^6	4.6×10^6	2.4	7.6	4.9×10^4	EIII3	4.9	0.13
J1331.0+5653	0.016	1.0	9.9×10^6	1.0×10^5	1.9	1.2	5.4×10^2	EIII3	5.2	0.41
J1336.2+2320	0.078	4.2	6.9×10^5	2.9×10^2	2.2	0.59	1.6×10^5	S0	5.2	0.57
J1340.8-0409	0.071	3.9	5.3×10^5	1.1×10^3	1.6	1.5	2.8×10^3	EII5	5.0	0.82
J1353.4+5600	8.7×10^{-3}	2.6×10^{-3}	4.0×10^6	1.2×10^4	2.4	0.58	5.5×10^4	S0	4.4	1.6
J1400.2-4010	0.56	11.0	5.1×10^5	1.9×10^8	2.1	1.3×10^{-4}	1.6×10^4	S0	4.9	0.56
J1419.3+0444	4.9×10^{-3}	2.0	6.6×10^7	3.5×10^5	2.2	2.3	8.2×10^4	EIII3	4.7	0.85
J1439.9-3953	0.24	7.2	2.6×10^6	7.3×10^6	2.6	3.2	9.8×10^5	S0	5.3	1.3
J1440.9+0609	0.014	6.8×10^{-3}	3.0×10^6	1.3×10^4	1.7	2.1	1.2×10^3	EII2	5.7	0.42
J1447.0-2657	0.18	5.8	2.4×10^7	2.0×10^6	1.3	10.0	1.1	EIII3	5.4	0.99
J1506.4-0540	0.030	4.3	2.4×10^6	6.0×10^5	1.4	3.8	3.5	S0	4.8	0.21
J1518.6+0614	0.052	2.1	4.8×10^6	4.0×10^5	2.0	2.3	6.2×10^2	EII5	5.9	0.27
J1532.0+3016	0.15	7.0	1.3×10^6	2.5×10^5	2.2	2.2	3.5×10^4	EIII3	4.4	26.0
J1533.2+1855	0.069	3.9	3.2×10^7	1.9×10^6	2.0	6.5	1.2×10^3	EIII3	5.4	0.85
J1533.2+3416	9.5×10^{-3}	9.4×10^{-3}	1.1×10^7	2.1×10^4	0.62	3.8	0.034	EII2	5.7	0.73
J1534.8+3716	0.011	1.3×10^{-3}	4.4×10^6	1.6×10^4	1.3	2.7	13.0	S0	4.7	0.43
J1539.7-1127	9.5×10^{-3}	1.3	1.1×10^7	2.3×10^6	2.3	6.5	3.7×10^4	EII5	5.0	0.80
J1554.4-1215	0.079	5.0	1.5×10^7	3.0×10^6	2.3	5.0	5.7×10^4	EII5	5.5	0.60
J1605.5+5423	0.34	10.0	3.5×10^6	2.2×10^6	2.0	4.0	8.0×10^3	EIII3	5.0	0.19
J1637.1+1316	0.79	9.9	4.6×10^7	6.2×10^5	2.2	8.5	5.4×10^4	S0	4.9	0.75
J1656.9-2010	0.27	8.0	6.5×10^6	8.5×10^5	1.7	8.5	3.2×10^2	EIII3	4.6	0.93
J1719.3+1205	0.036	3.0	8.0×10^6	4.0×10^5	1.6	2.9	1.2×10^2	EII2	5.5	1.1
J1757.0+7032	0.16	4.0	1.7×10^7	1.7×10^5	1.9	2.5	3.8×10^2	S0	4.4	0.40
J1808.8+2419	0.15	5.4	2.6×10^6	3.4×10^6	1.9	2.1	2.9×10^3	S0	4.6	0.82
J1824.5+4311	1.9	7.8	8.7×10^7	5.7×10^4	1.1	2.2	1.2	S0	4.7	0.50
J1841.3+2909	0.062	3.0	1.1×10^8	8.8×10^5	2.0	3.5	5.2×10^3	EII5	5.3	0.75
J1848.5+6537	0.016	2.0	7.9×10^7	9.0×10^5	1.7	2.8	1.6×10^2	S0	4.3	0.46
J1850.5+2631	4.3×10^{-3}	1.9×10^{-4}	5.8×10^6	1.8×10^6	1.8	6.5	1.7×10^2	S0	3.8	0.52
J1923.4-2503	0.069	8.0	2.3×10^7	5.1×10^5	1.4	1.9	10.0	S0	5.2	0.46
J1944.4-4523	0.12	3.7	1.2×10^7	1.4×10^5	1.2	4.2	1.2	EIII3	5.0	0.32
J1954.9-5640	0.031	2.9×10^{-4}	8.6×10^6	1.2×10^5	2.2	2.3	1.1×10^4	S0	3.8	0.88
J2015.0+1621	0.027	3.0	1.5×10^7	2.9×10^6	2.3	6.5	8.5×10^4	S0	5.1	2.7
J2022.0-7224	0.10	3.0	1.6×10^7	6.6×10^5	2.4	2.5	1.2×10^5	S0	5.3	0.52
J2030.9+1935	0.11	5.4	1.9×10^7	1.6×10^5	2.1	2.6	1.2×10^4	S0	5.2	0.60
J2034.8-4200	0.21	5.1	3.2×10^6	2.2×10^4	0.73	3.8	0.097	EII2	5.3	0.24
J2040.1-4621	0.12	3.0	2.0×10^7	4.0×10^5	2.1	2.5	4.4×10^3	EIII3	5.4	0.51
J2041.9-3735	0.22	7.6	1.1×10^7	3.6×10^6	1.8	6.5	4.4×10^2	S0	4.5	1.2
J2052.5+0810	0.14	8.0	1.9×10^7	5.6×10^5	0.54	7.1	1.3×10^{-3}	S0	4.8	0.37
J2112.7+0819	0.45	6.3	1.1×10^6	2.9×10^5	2.2	2.8	7.5×10^4	EII2	5.2	0.93
J2145.7+0718	1.7	7.3	1.9×10^7	2.3×10^6	2.4	6.4	5.4×10^4	EIII3	5.1	0.46
J2232.6-2023	0.20	3.0	2.0×10^7	1.5×10^6	1.9	6.5	5.6×10^2	EIII3	4.4	1.6
J2246.7-5207	0.28	3.8	6.1×10^6	1.3×10^6	1.7	6.5	46.0	EIII3	4.9	0.59
J2258.4-5524	0.36	3.3	1.8×10^6	3.9×10^5	2.3	6.5	6.0×10^4	EIII3	4.7	0.49
J2306.6-1105	2.6	7.0	1.8×10^6	1.9×10^6	2.3	3.7	3.6×10^4	S0	4.6	1.1
J2319.1-4207	0.36	7.3	1.5×10^6	1.9×10^4	1.6	1.9	1.4×10^2	EIII3	4.3	1.1
J2340.8+8015	0.027	1.0	1.1×10^7	1.1×10^5	1.7	3.8	6.8×10^2	EII2	5.2	0.38
J2356.2+4036	6.7×10^{-3}	1.0	1.9×10^6	1.0×10^3	1.8	0.98	6.0×10^3	EIII3	3.6	0.53

Table B.2: Results for the synchrotron peak frequency $\nu_{\text{sync}}^{\text{peak}}$ and CD obtained from the broadband SED modelling, along with the energy budget results, are presented. These include the luminosity carried by the jet for the non-thermal low-energy and total radiative components, L_{sync} and L_{rad} , the luminosities of the electrons L_{kin} and the magnetic fields L_B , the total jet luminosity L_{tot} , and the ratio of the magnetic to electron energy density U_B/U_e .

4FGL Name	$\nu_{\text{sync}}^{\text{peak}}$ [Hz]	CD	L_{sync} [erg s ⁻¹]	L_{rad} [erg s ⁻¹]	L_B [erg s ⁻¹]	L_{kin} [erg s ⁻¹]	L_{tot} [erg s ⁻¹]	U_B/U_e
J0003.1–5248	2.5×10^{17}	0.69	4.3×10^{42}	6.9×10^{42}	2.3×10^{42}	1.4×10^{47}	1.4×10^{47}	0.033
J0008.4–2339	6.7×10^{16}	0.22	4.3×10^{40}	5.1×10^{40}	1.2×10^{41}	5.8×10^{44}	5.8×10^{44}	0.012
J0013.9–1854	9.5×10^{17}	0.16	5.0×10^{41}	6.0×10^{41}	6.0×10^{41}	1.0×10^{46}	1.0×10^{46}	0.035
J0029.4+2051	4.3×10^{17}	0.91	2.9×10^{43}	5.0×10^{43}	2.1×10^{42}	1.7×10^{44}	2.2×10^{44}	0.021
J0039.1–2219	1.2×10^{18}	1.2	5.5×10^{42}	1.4×10^{43}	3.5×10^{40}	4.5×10^{44}	4.6×10^{44}	1.4×10^{-4}
J0049.5–4150	7.3×10^{17}	0.80	2.5×10^{45}	4.1×10^{45}	5.3×10^{43}	3.2×10^{44}	4.5×10^{45}	0.18
J0054.7–2455	1.0×10^{16}	0.42	7.7×10^{41}	1.1×10^{42}	1.9×10^{42}	5.5×10^{43}	5.8×10^{43}	0.069
J0059.3–0152	7.3×10^{17}	0.40	2.1×10^{44}	2.8×10^{44}	1.0×10^{43}	1.0×10^{44}	3.9×10^{44}	0.096
J0102.7–2001	1.9×10^{17}	0.32	1.6×10^{41}	2.0×10^{41}	1.9×10^{41}	5.4×10^{44}	5.4×10^{44}	0.012
J0121.8–3916	6.7×10^{19}	0.26	3.4×10^{44}	4.2×10^{44}	1.3×10^{44}	1.0×10^{45}	1.6×10^{45}	2.0
J0123.7–2311	9.5×10^{17}	0.34	1.1×10^{42}	1.5×10^{42}	6.1×10^{41}	8.2×10^{45}	8.2×10^{45}	0.020
J0127.1+3310	2.1×10^{18}	0.37	1.6×10^{44}	2.1×10^{44}	4.3×10^{43}	2.8×10^{46}	2.8×10^{46}	0.62
J0132.7–0804	4.3×10^{17}	0.27	1.2×10^{44}	1.6×10^{44}	1.0×10^{44}	5.0×10^{44}	7.6×10^{44}	2.1
J0146.9–5202	9.4×10^{14}	0.61	1.3×10^{40}	2.1×10^{40}	3.0×10^{40}	5.7×10^{46}	5.7×10^{46}	6.3×10^{-4}
J0150.6–5448	7.9×10^{15}	0.32	7.3×10^{39}	9.2×10^{39}	2.8×10^{40}	3.0×10^{44}	3.0×10^{44}	1.8×10^{-3}
J0202.4+0849	1.9×10^{17}	1.3	5.0×10^{45}	9.3×10^{45}	1.4×10^{44}	3.4×10^{44}	9.8×10^{45}	0.42
J0212.2–2559	1.5×10^{17}	0.77	1.2×10^{44}	2.0×10^{44}	4.1×10^{43}	5.7×10^{45}	6.0×10^{45}	0.45
J0216.5+2313	8.7×10^{16}	0.39	3.3×10^{43}	4.5×10^{43}	3.9×10^{43}	1.2×10^{46}	1.2×10^{46}	0.91
J0233.9+8041	1.9×10^{17}	0.99	1.1×10^{43}	1.9×10^{43}	9.8×10^{41}	7.4×10^{43}	9.3×10^{43}	0.013
J0241.9–1603	7.9×10^{15}	0.54	4.1×10^{41}	6.2×10^{41}	8.4×10^{41}	9.8×10^{43}	9.9×10^{43}	0.029
J0304.5–0054	1.1×10^{17}	0.59	3.0×10^{41}	4.5×10^{41}	5.0×10^{41}	1.3×10^{48}	1.3×10^{48}	9.7×10^{-3}
J0305.1–1608	1.5×10^{17}	0.53	2.1×10^{42}	3.2×10^{42}	1.7×10^{42}	5.3×10^{45}	5.4×10^{45}	0.044
J0309.4–4000	3.3×10^{17}	0.56	7.8×10^{43}	1.3×10^{44}	8.0×10^{42}	2.1×10^{45}	2.2×10^{45}	0.074
J0314.3+0620	8.7×10^{16}	0.27	2.5×10^{43}	3.0×10^{43}	4.8×10^{43}	1.4×10^{44}	2.2×10^{44}	2.1
J0323.7–0111	8.8×10^{19}	0.49	1.5×10^{47}	2.5×10^{47}	5.6×10^{44}	3.0×10^{45}	2.5×10^{47}	0.62
J0330.7–2408	1.1×10^{17}	0.53	2.3×10^{42}	3.8×10^{42}	1.4×10^{42}	5.6×10^{45}	5.6×10^{45}	0.030
J0336.5–0348	2.8×10^{18}	0.84	8.1×10^{41}	1.4×10^{42}	1.1×10^{40}	1.2×10^{44}	1.2×10^{44}	1.1×10^{-4}
J0357.2–0319	1.2×10^{18}	0.71	1.6×10^{44}	2.9×10^{44}	3.3×10^{42}	8.3×10^{44}	1.1×10^{45}	0.015
J0359.0–3053	1.1×10^{17}	0.31	2.4×10^{43}	3.1×10^{43}	3.1×10^{43}	2.0×10^{44}	2.7×10^{44}	1.1
J0409.4+3201	5.6×10^{17}	0.70	1.5×10^{42}	2.7×10^{42}	1.4×10^{41}	6.2×10^{44}	6.2×10^{44}	2.1×10^{-3}
J0420.3–6016	5.1×10^{16}	0.55	1.8×10^{42}	2.6×10^{42}	2.2×10^{42}	1.6×10^{46}	1.6×10^{46}	0.056
J0429.3–3238	5.1×10^{16}	0.27	1.0×10^{43}	1.3×10^{43}	2.8×10^{43}	3.4×10^{45}	3.5×10^{45}	1.2
J0440.8+2749	5.1×10^{16}	2.5	3.3×10^{43}	1.2×10^{44}	7.0×10^{42}	5.7×10^{46}	5.7×10^{46}	0.032
J0441.5+1505	1.6×10^{18}	0.096	7.7×10^{44}	8.4×10^{44}	6.7×10^{42}	2.1×10^{44}	1.1×10^{45}	0.032
J0503.5–1116	1.1×10^{17}	0.59	1.3×10^{42}	2.0×10^{42}	1.3×10^{42}	2.0×10^{46}	2.0×10^{46}	0.03
J0505.6+0415	1.4×10^{16}	0.58	6.9×10^{41}	1.1×10^{42}	1.3×10^{42}	2.0×10^{46}	2.0×10^{46}	0.032
J0506.9+0323	1.8×10^{16}	1.4	8.6×10^{43}	1.9×10^{44}	4.8×10^{43}	1.7×10^{46}	1.7×10^{46}	0.36
J0509.6–0402	7.3×10^{17}	0.11	1.3×10^{45}	1.4×10^{45}	1.2×10^{45}	4.3×10^{44}	3.0×10^{45}	39.0
J0526.7–1519	1.0×10^{16}	0.83	6.1×10^{40}	1.1×10^{41}	8.4×10^{40}	5.8×10^{45}	5.8×10^{45}	2.0×10^{-3}
J0536.4–3343	3.9×10^{16}	0.74	7.1×10^{42}	1.2×10^{43}	5.7×10^{42}	3.8×10^{43}	5.5×10^{43}	0.15
J0537.7–5717	1.0×10^{16}	0.68	7.5×10^{42}	1.3×10^{43}	1.2×10^{43}	9.8×10^{43}	1.2×10^{44}	0.26
J0557.3–0615	2.1×10^{18}	0.18	4.4×10^{44}	5.1×10^{44}	7.6×10^{43}	2.3×10^{44}	8.1×10^{44}	1.5
J0558.0–3837	1.1×10^{17}	0.19	4.7×10^{42}	5.5×10^{42}	1.5×10^{43}	2.7×10^{45}	2.7×10^{45}	0.91
J0606.5–4730	3.3×10^{17}	0.71	5.9×10^{44}	1.0×10^{45}	7.9×10^{43}	4.8×10^{45}	5.9×10^{45}	0.54
J0611.1+4325	6.7×10^{16}	1.4	1.9×10^{43}	4.2×10^{43}	5.1×10^{42}	9.0×10^{44}	9.4×10^{44}	0.051
J0644.6–2853	5.1×10^{16}	0.45	9.3×10^{43}	1.3×10^{44}	5.9×10^{43}	8.5×10^{43}	2.7×10^{44}	1.3
J0730.4+3308	1.0×10^{16}	0.36	5.8×10^{42}	7.4×10^{42}	1.4×10^{43}	2.7×10^{43}	4.9×10^{43}	0.58
J0731.9+2805	4.3×10^{17}	0.25	3.7×10^{40}	4.8×10^{40}	7.0×10^{40}	1.5×10^{47}	1.5×10^{47}	3.1×10^{-3}
J0737.3–8247	1.4×10^{16}	1.5	1.9×10^{41}	4.7×10^{41}	1.3×10^{41}	1.4×10^{47}	1.4×10^{47}	1.3×10^{-3}
J0748.3+8511	4.3×10^{17}	0.57	2.3×10^{44}	3.4×10^{44}	1.6×10^{43}	1.5×10^{44}	5.0×10^{44}	0.14
J0759.6+1321	3.9×10^{16}	0.25	3.5×10^{43}	4.2×10^{43}	5.4×10^{43}	2.0×10^{43}	1.2×10^{44}	2.7
J0804.9–0624	3.3×10^{17}	0.55	1.2×10^{42}	1.8×10^{42}	8.1×10^{41}	5.8×10^{46}	5.8×10^{46}	0.017
J0813.7–0356	2.5×10^{17}	0.71	1.3×10^{44}	2.5×10^{44}	6.2×10^{42}	5.2×10^{44}	7.7×10^{44}	0.038
J0819.4–0756	8.0×10^{18}	0.13	6.4×10^{43}	7.4×10^{43}	1.4×10^{43}	1.3×10^{46}	1.4×10^{46}	0.35
J0829.0+1755	1.1×10^{17}	0.21	1.2×10^{45}	1.4×10^{45}	1.3×10^{45}	1.5×10^{45}	4.2×10^{45}	34.0
J0842.5+0251	1.8×10^{16}	0.95	8.0×10^{40}	1.6×10^{41}	8.5×10^{40}	5.7×10^{45}	5.7×10^{45}	1.9×10^{-3}
J0850.5+3455	3.6×10^{15}	1.0	1.9×10^{40}	4.1×10^{40}	2.5×10^{40}	1.7×10^{46}	1.7×10^{46}	4.5×10^{-4}
J0908.9+2311	4.7×10^{15}	1.1	8.4×10^{39}	1.8×10^{40}	8.8×10^{39}	5.4×10^{43}	5.4×10^{43}	2.6×10^{-4}
J0912.9–2102	5.6×10^{17}	0.63	5.0×10^{42}	8.0×10^{42}	9.3×10^{41}	1.9×10^{45}	1.9×10^{45}	0.015
J0920.9–2256	9.5×10^{17}	0.18	8.0×10^{44}	8.9×10^{44}	2.3×10^{44}	1.0×10^{44}	1.2×10^{45}	5.7
J0924.0+0534	1.9×10^{17}	0.20	5.3×10^{40}	6.7×10^{40}	1.2×10^{41}	1.7×10^{46}	1.7×10^{46}	7.4×10^{-3}
J0954.2+4913	5.1×10^{16}	1.0	5.4×10^{42}	9.8×10^{42}	9.9×10^{41}	5.3×10^{43}	6.4×10^{43}	0.019
J0956.5–0958	1.6×10^{18}	0.39	2.0×10^{44}	2.7×10^{44}	3.1×10^{42}	1.7×10^{44}	4.4×10^{44}	0.019

Continued on next page

Table B.2: *continued*

4FGL Name	$\nu_{\text{sync}}^{\text{peak}}$ [Hz]	CD	L_{sync} [erg s ⁻¹]	L_{rad} [erg s ⁻¹]	L_B [erg s ⁻¹]	L_{kin} [erg s ⁻¹]	L_{tot} [erg s ⁻¹]	U_B/U_e
J1021.1+1626	3.6×10^{18}	0.40	1.7×10^{43}	2.2×10^{43}	1.6×10^{43}	1.3×10^{47}	1.3×10^{47}	0.33
J1107.8+1501	1.8×10^{16}	1.2	1.6×10^{42}	3.6×10^{42}	1.3×10^{42}	8.2×10^{45}	8.2×10^{45}	0.017
J1123.8+7230	7.3×10^{17}	0.21	2.1×10^{43}	2.5×10^{43}	5.4×10^{42}	1.4×10^{44}	1.8×10^{44}	0.17
J1132.2-4736	2.3×10^{19}	0.19	2.9×10^{45}	3.4×10^{45}	8.4×10^{43}	3.7×10^{45}	7.2×10^{45}	0.60
J1213.3-2618	5.6×10^{17}	0.32	8.1×10^{41}	1.0×10^{42}	4.0×10^{41}	1.0×10^{44}	1.0×10^{44}	0.019
J1225.3-3446	1.5×10^{20}	0.14	1.3×10^{44}	1.5×10^{44}	5.5×10^{43}	6.2×10^{47}	6.2×10^{47}	0.99
J1231.5+1421	1.4×10^{16}	0.86	9.2×10^{41}	1.6×10^{42}	9.3×10^{41}	5.0×10^{44}	5.0×10^{44}	0.020
J1236.3+3858	3.6×10^{15}	1.0	7.4×10^{40}	1.6×10^{41}	9.7×10^{40}	3.5×10^{46}	3.5×10^{46}	1.4×10^{-3}
J1237.8+6256	5.1×10^{16}	0.22	1.0×10^{40}	1.2×10^{40}	3.6×10^{40}	1.6×10^{45}	1.6×10^{45}	3.7×10^{-3}
J1241.8-1456	9.4×10^{14}	0.33	1.7×10^{40}	2.3×10^{40}	7.0×10^{40}	2.1×10^{43}	2.1×10^{43}	3.4×10^{-3}
J1253.5-3934	1.0×10^{19}	0.079	1.9×10^{45}	1.9×10^{45}	2.0×10^{44}	4.0×10^{43}	2.2×10^{45}	5.0
J1256.2-1146	2.3×10^{16}	0.72	1.3×10^{42}	2.1×10^{42}	1.3×10^{42}	1.4×10^{45}	1.4×10^{45}	0.032
J1310.2-1158	8.7×10^{16}	1.3	1.8×10^{42}	3.9×10^{42}	6.8×10^{41}	5.4×10^{46}	5.4×10^{46}	7.4×10^{-3}
J1311.0+0034	2.5×10^{14}	1.2	6.4×10^{38}	1.4×10^{39}	7.4×10^{38}	2.3×10^{44}	2.3×10^{44}	1.9×10^{-5}
J1326.1+1232	1.9×10^{17}	0.28	1.3×10^{40}	1.7×10^{40}	2.7×10^{40}	2.8×10^{46}	2.8×10^{46}	1.6×10^{-3}
J1331.0+5653	6.2×10^{18}	0.59	1.3×10^{41}	1.9×10^{41}	3.7×10^{40}	3.3×10^{44}	3.3×10^{44}	1.3×10^{-3}
J1336.2+2320	1.9×10^{17}	0.55	5.1×10^{41}	7.8×10^{41}	9.2×10^{41}	9.3×10^{46}	9.3×10^{46}	0.017
J1340.8-0409	4.2×10^{14}	0.89	4.3×10^{41}	7.7×10^{41}	7.5×10^{41}	1.7×10^{45}	1.7×10^{45}	9.2×10^{-3}
J1353.4+5600	1.2×10^{18}	0.43	5.8×10^{39}	7.9×10^{39}	1.1×10^{40}	3.1×10^{46}	3.1×10^{46}	4.5×10^{-4}
J1400.2-4010	4.3×10^{17}	0.37	2.7×10^{44}	3.9×10^{44}	4.8×10^{43}	9.2×10^{45}	9.6×10^{45}	0.51
J1419.3+0444	1.0×10^{16}	3.2	1.2×10^{40}	5.0×10^{40}	3.6×10^{39}	4.6×10^{46}	4.6×10^{46}	3.0×10^{-5}
J1439.9-3953	2.8×10^{18}	0.58	2.4×10^{43}	3.9×10^{43}	8.8×10^{42}	5.6×10^{47}	5.6×10^{47}	0.091
J1440.9+0609	7.2×10^{14}	0.66	1.4×10^{40}	2.6×10^{40}	3.1×10^{40}	7.1×10^{44}	7.1×10^{44}	6.4×10^{-4}
J1447.0-2657	7.3×10^{17}	0.12	1.8×10^{43}	2.0×10^{43}	5.0×10^{42}	2.3×10^{43}	4.8×10^{43}	0.23
J1506.4-0540	2.5×10^{17}	0.58	7.1×10^{41}	1.1×10^{42}	1.3×10^{41}	3.4×10^{43}	3.5×10^{43}	4.2×10^{-3}
J1518.6+0614	3.3×10^{17}	0.12	1.6×10^{41}	1.8×10^{41}	4.0×10^{41}	3.6×10^{44}	3.6×10^{44}	0.055
J1532.0+3016	5.1×10^{16}	0.95	6.7×10^{42}	1.2×10^{43}	3.6×10^{42}	2.0×10^{46}	2.0×10^{46}	0.047
J1533.2+1855	3.3×10^{17}	0.34	1.4×10^{42}	1.8×10^{42}	7.2×10^{41}	6.9×10^{44}	6.9×10^{44}	0.027
J1533.2+3416	1.6×10^{15}	0.69	6.8×10^{39}	1.2×10^{40}	1.3×10^{40}	2.3×10^{43}	2.3×10^{43}	5.8×10^{-4}
J1534.8+3716	9.4×10^{14}	0.57	7.2×10^{39}	1.2×10^{40}	1.8×10^{40}	3.6×10^{43}	3.6×10^{43}	6.2×10^{-4}
J1539.7-1127	6.7×10^{16}	0.91	1.9×10^{40}	3.7×10^{40}	1.4×10^{40}	2.1×10^{46}	2.1×10^{46}	3.2×10^{-4}
J1554.4-1215	4.3×10^{17}	0.51	1.9×10^{42}	2.8×10^{42}	9.3×10^{41}	3.3×10^{46}	3.3×10^{46}	0.019
J1605.5+5423	1.2×10^{18}	0.47	1.8×10^{44}	2.5×10^{44}	1.7×10^{43}	4.6×10^{45}	4.9×10^{45}	0.17
J1637.1+1316	2.3×10^{16}	0.71	1.0×10^{44}	1.7×10^{44}	9.4×10^{43}	3.1×10^{46}	3.1×10^{46}	1.2
J1656.9-2010	8.7×10^{16}	1.2	6.1×10^{43}	1.3×10^{44}	1.1×10^{43}	2.9×10^{44}	4.3×10^{44}	0.095
J1719.3+1205	2.5×10^{17}	1.5	1.7×10^{42}	3.8×10^{42}	1.9×10^{41}	1.5×10^{44}	1.5×10^{44}	2.5×10^{-3}
J1757.0+7032	1.1×10^{17}	0.17	1.7×10^{42}	1.9×10^{42}	3.6×10^{42}	2.3×10^{44}	2.3×10^{44}	0.30
J1808.8+2419	6.2×10^{18}	0.35	8.8×10^{43}	1.2×10^{44}	3.4×10^{42}	1.7×10^{45}	1.9×10^{45}	0.032
J1824.5+4311	2.8×10^{18}	0.18	5.0×10^{45}	5.4×10^{45}	5.3×10^{44}	6.5×10^{43}	6.0×10^{45}	8.3
J1841.3+2909	3.3×10^{17}	0.93	2.4×10^{42}	4.4×10^{42}	5.8×10^{41}	3.0×10^{45}	3.0×10^{45}	8.9×10^{-3}
J1848.5+6537	5.6×10^{17}	1.1	5.0×10^{41}	9.5×10^{41}	3.9×10^{40}	1.5×10^{44}	1.5×10^{44}	6.4×10^{-4}
J1850.5+2631	8.7×10^{16}	1.0	6.8×10^{39}	1.3×10^{40}	2.7×10^{39}	1.2×10^{44}	1.2×10^{44}	1.2×10^{-4}
J1923.4-2503	8.0×10^{18}	0.45	6.2×10^{43}	8.0×10^{43}	7.1×10^{41}	1.4×10^{44}	2.2×10^{44}	5.5×10^{-3}
J1944.4-4523	6.7×10^{16}	0.52	3.0×10^{42}	4.3×10^{42}	2.3×10^{42}	2.7×10^{43}	3.3×10^{43}	0.088
J1954.9-5640	1.8×10^{16}	0.55	7.3×10^{40}	1.1×10^{41}	1.4×10^{41}	6.0×10^{45}	6.0×10^{45}	4.8×10^{-3}
J2015.0+1621	1.5×10^{17}	1.7	4.4×10^{41}	1.2×10^{42}	1.1×10^{41}	4.8×10^{46}	4.8×10^{46}	1.0×10^{-3}
J2022.0-7224	1.9×10^{17}	0.48	1.3×10^{42}	1.9×10^{42}	1.5×10^{42}	6.8×10^{46}	6.8×10^{46}	0.037
J2030.9+1935	2.3×10^{16}	1.3	3.8×10^{42}	8.2×10^{42}	2.0×10^{42}	7.1×10^{45}	7.1×10^{45}	0.023
J2034.8-4200	7.9×10^{15}	0.45	3.1×10^{42}	4.4×10^{42}	6.9×10^{42}	2.4×10^{43}	3.5×10^{43}	0.29
J2040.1-4621	3.3×10^{17}	0.38	3.1×10^{42}	4.0×10^{42}	2.2×10^{42}	2.5×10^{45}	2.5×10^{45}	0.072
J2041.9-3735	2.1×10^{18}	0.29	1.0×10^{44}	1.3×10^{44}	7.3×10^{42}	3.2×10^{44}	4.6×10^{44}	0.10
J2052.5+0810	1.9×10^{17}	0.47	3.4×10^{43}	4.6×10^{43}	3.0×10^{42}	6.5×10^{43}	1.1×10^{44}	0.047
J2112.7+0819	8.7×10^{16}	1.1	6.7×10^{43}	1.3×10^{44}	3.0×10^{43}	4.2×10^{46}	4.3×10^{46}	0.27
J2145.7+0718	1.2×10^{18}	0.15	4.1×10^{44}	4.6×10^{44}	4.3×10^{44}	3.1×10^{46}	3.2×10^{46}	12.0
J2232.6-2023	7.3×10^{17}	0.21	9.0×10^{42}	1.1×10^{43}	5.8×10^{42}	3.4×10^{44}	3.6×10^{44}	0.26
J2246.7-5207	9.5×10^{17}	0.082	1.2×10^{43}	1.3×10^{43}	1.1×10^{43}	3.8×10^{43}	6.2×10^{43}	0.98
J2258.4-5524	2.3×10^{16}	0.46	9.0×10^{42}	1.3×10^{43}	1.9×10^{43}	3.4×10^{46}	3.4×10^{46}	0.45
J2306.6-1105	6.2×10^{18}	0.093	1.2×10^{45}	1.3×10^{45}	9.8×10^{44}	2.0×10^{46}	2.2×10^{46}	31.0
J2319.1-4207	1.8×10^{16}	0.37	1.1×10^{43}	1.3×10^{43}	1.9×10^{43}	1.1×10^{44}	1.4×10^{44}	0.70
J2340.8+8015	7.9×10^{15}	2.0	1.9×10^{41}	6.0×10^{41}	1.1×10^{41}	4.7×10^{44}	4.7×10^{44}	1.3×10^{-3}
J2356.2+4036	4.3×10^{17}	1.4	1.4×10^{40}	3.7×10^{40}	6.7×10^{39}	3.5×10^{45}	3.5×10^{45}	6.9×10^{-5}